EUROPEAN LABORATORY FOR PARTICLE PHYSICS (CERN)

CERN-PPE/93-39
10 March, 1993

Measurement of the Tau Polarisation at the Z Resonance

The ALEPH Collaboration

Abstract

Using 18.8 pb^{-1} of data collected in 1990 and 1991, ALEPH has measured the tau polarisation in the decay modes $\tau \to e\nu\bar{\nu}$, $\tau \to \mu\nu\bar{\nu}$, $\tau \to \pi\nu$, $\tau \to \rho\nu$ and $\tau \to a_1\nu$, using both the individual tau decay kinematics and the event acollinearity. The measurement of the tau polarisation as a function of the production polar angle yields the two parameters $\mathcal{A}_\tau$ and $\mathcal{A}_e$, where $\mathcal{A}_l = 2g_V^l g_A^l/[(g_V^l)^2 + (g_A^l)^2]$. The results $\mathcal{A}_\tau = 0.143 \pm 0.023$ and $\mathcal{A}_e = 0.120 \pm 0.026$ are consistent with the hypothesis of electron-tau universality. Assuming universality yields a measurement of the effective weak mixing angle $\sin^2\theta_W^{\rm eff} = 0.2332 \pm 0.0022$.

Submitted to Zeitschrift für Physik C

The ALEPH Collaboration

D. Buskulic, D. Decamp, C. Goy, J.-P. Lees, M.-N. Minard, B. Mours, B. Pietrzyk

Laboratoire de Physique des Particules (LAPP), IN^2P^3-CNRS, 74019 Annecy-le-Vieux Cedex, France

R. Alemany, F. Ariztizabal, P. Comas, J.M. Crespo, M. Delfino, E. Fernandez, M. Fernandez-Bosman, V. Gaitan, Ll. Garrido, T. Mattison, A. Pacheco, C. Padilla, A. Pascual

Institut de Fisica d'Altes Energies, Universitat Autonoma de Barcelona, 08193 Bellaterra (Barcelona), Spain[7]

D. Creanza, M. de Palma, A. Farilla, G. Iaselli, G. Maggi, M. Maggi, S. Natali, S. Nuzzo, M. Quattromini, A. Ranieri, G. Raso, F. Romano, F. Ruggieri, G. Selvaggi, L. Silvestris, P. Tempesta, G. Zito

INFN Sezione di Bari e Dipartimento di Fisica dell' Università, 70126 Bari, Italy

Y. Chai, H. Hu, D. Huang, X. Huang, J. Lin, T. Wang, Y. Xie, D. Xu, R. Xu, J. Zhang, L. Zhang, W. Zhao

Institute of High-Energy Physics, Academia Sinica, Beijing, The People's Republic of China[8]

L.A.T. Bauerdick,[23] E. Blucher, G. Bonvicini, J. Boudreau, D. Casper, H. Drevermann, R.W. Forty, G. Ganis, C. Gay, R. Hagelberg, J. Harvey, S. Haywood, J. Hilgart, R. Jacobsen, B. Jost, J. Knobloch, I. Lehraus, T. Lohse,[29] A. Lusiani, M. Martinez, P. Mato, H. Meinhard, A. Minten, A. Miotto, R. Miquel, H.-G. Moser, P. Palazzi, J.A. Perlas, J.-F. Pusztaszeri, F. Ranjard, G. Redlinger,[24] L. Rolandi, J. Rothberg,[2] T. Ruan, M. Saich, D. Schlatter, M. Schmelling, F. Sefkow, W. Tejessy, H. Wachsmuth, W. Wiedenmann, T. Wildish, W. Witzeling, J. Wotschack

European Laboratory for Particle Physics (CERN), 1211 Geneva 23, Switzerland

Z. Ajaltouni, F. Badaud, M. Bardadin-Otwinowska, R. El Fellous, A. Falvard, P. Gay, C. Guicheney, P. Henrard, J. Jousset, B. Michel, J-C. Montret, D. Pallin, P. Perret, F. Podlyski, J. Proriol, F. Prulhière, F. Saadi

Laboratoire de Physique Corpusculaire, Université Blaise Pascal, IN^2P^3-CNRS, Clermont-Ferrand, 63177 Aubière, France

T. Fearnley, J.D. Hansen, J.R. Hansen,[1] P.H. Hansen, R. Møllerud, B.S. Nilsson[1]

Niels Bohr Institute, 2100 Copenhagen, Denmark[9]

I. Efthymiopoulos, A. Kyriakis, E. Simopoulou, A. Vayaki, K. Zachariadou

Nuclear Research Center Demokritos (NRCD), Athens, Greece

J. Badier, A. Blondel, G. Bonneaud, J.C. Brient, G. Fouque, S. Orteu, A. Rougé, M. Rumpf, R. Tanaka, M. Verderi, H. Videau

Laboratoire de Physique Nucléaire et des Hautes Energies, Ecole Polytechnique, IN^2P^3-CNRS, 91128 Palaiseau Cedex, France

D.J. Candlin, M.I. Parsons, E. Veitch

Department of Physics, University of Edinburgh, Edinburgh EH9 3JZ, United Kingdom[10]

L. Moneta, G. Parrini

Dipartimento di Fisica, Università di Firenze, INFN Sezione di Firenze, 50125 Firenze, Italy

M. Corden, C. Georgiopoulos, M. Ikeda, J. Lannutti, D. Levinthal,[15] M. Mermikides†, L. Sawyer, S. Wasserbaech

Supercomputer Computations Research Institute and Dept. of Physics, Florida State University, Tallahassee, FL 32306, USA [12,13,14]

A. Antonelli, R. Baldini, G. Bencivenni, G. Bologna,[4] F. Bossi, P. Campana, G. Capon, F. Cerutti, V. Chiarella, B. D'Ettorre-Piazzoli,[25] G. Felici, P. Laurelli, G. Mannocchi,[5] F. Murtas, G.P. Murtas, L. Passalacqua, M. Pepe-Altarelli, P. Picchi[4]

Laboratori Nazionali dell'INFN (LNF-INFN), 00044 Frascati, Italy

P. Colrain, I. ten Have, J.G. Lynch, W. Maitland, W.T. Morton, C. Raine, P. Reeves, J.M. Scarr, K. Smith, M.G. Smith, A.S. Thompson, R.M. Turnbull

Department of Physics and Astronomy, University of Glasgow, Glasgow G12 8QQ,United Kingdom[10]

B. Brandl, O. Braun, C. Geweniger, P. Hanke, V. Hepp, E.E. Kluge, Y. Maumary, A. Putzer, B. Rensch, A. Stahl, K. Tittel, M. Wunsch

Institut für Hochenergiephysik, Universität Heidelberg, 6900 Heidelberg, Fed. Rep. of Germany[16]

A.T. Belk, R. Beuselinck, D.M. Binnie, W. Cameron, M. Cattaneo, D.J. Colling, P.J. Dornan, S. Dugeay, A.M. Greene, J.F. Hassard, N.M. Lieske,[31] J. Nash, D.G. Payne, M.J. Phillips, J.K. Sedgbeer, I.R. Tomalin, A.G. Wright

Department of Physics, Imperial College, London SW7 2BZ, United Kingdom[10]

P. Girtler, E. Kneringer, D. Kuhn, G. Rudolph

Institut für Experimentalphysik, Universität Innsbruck, 6020 Innsbruck, Austria[18]

C.K. Bowdery, T.J. Brodbeck, A.J. Finch, F. Foster, G. Hughes, D. Jackson, N.R. Keemer, M. Nuttall, A. Patel, T. Sloan, S.W. Snow, E.P. Whelan

Department of Physics, University of Lancaster, Lancaster LA1 4YB, United Kingdom[10]

K. Kleinknecht, J. Raab, B. Renk, H.-G. Sander, H. Schmidt, F. Steeg, S.M. Walther, R. Wanke, B. Wolf

Institut für Physik, Universität Mainz, 6500 Mainz, Fed. Rep. of Germany[16]

J-J. Aubert, A.M. Bencheikh, C. Benchouk, A. Bonissent, J. Carr, P. Coyle, J. Drinkard,[3] F. Etienne, D. Nicod, S. Papalexiou, P. Payre, L. Roos, D. Rousseau, P. Schwemling, M. Talby

Centre de Physique des Particules, Faculté des Sciences de Luminy, IN^{2}P^3-CNRS, 13288 Marseille, France

S. Adlung, R. Assmann, C. Bauer, W. Blum, D. Brown, P. Cattaneo,[28] B. Dehning, H. Dietl, F. Dydak,[22] M. Frank, A.W. Halley, J. Lauber, G. Lütjens, G. Lutz, W. Männer, R. Richter, H. Rotscheidt, J. Schröder, A.S. Schwarz, R. Settles, H. Seywerd, U. Stierlin, U. Stiegler, R. St. Denis, G. Wolf

Max-Planck-Institut für Physik, Werner-Heisenberg-Institut, 8000 München, Fed. Rep. of Germany[16]

J. Boucrot,[1] O. Callot, A. Cordier, M. Davier, L. Duflot, J.-F. Grivaz, Ph. Heusse, D.E. Jaffe, P. Janot, D.W. Kim,[19] F. Le Diberder, J. Lefrançois, A.-M. Lutz, M.-H. Schune, J.-J. Veillet, I. Videau, Z. Zhang,

Laboratoire de l'Accélérateur Linéaire, Université de Paris-Sud, IN^{2}P^3-CNRS, 91405 Orsay Cedex, France

D. Abbaneo, G. Bagliesi, G. Batignani, L. Bosisio, U. Bottigli, C. Bozzi, G. Calderini, M. Carpinelli, M.A. Ciocci, R. Dell'Orso, I. Ferrante, F. Fidecaro, L. Foà, E. Focardi, F. Forti, A. Giassi, M.A. Giorgi, A. Gregorio, F. Ligabue, E.B. Mannelli, P.S. Marrocchesi, A. Messineo, F. Palla, G. Rizzo, G. Sanguinetti, P. Spagnolo, J. Steinberger, R. Tenchini, G. Tonelli, G. Triggiani, C. Vannini, A. Venturi, P.G. Verdini, J. Walsh

Dipartimento di Fisica dell'Università, INFN Sezione di Pisa, e Scuola Normale Superiore, 56010 Pisa, Italy

A.P. Betteridge, J.M. Carter, M.G. Green, P.V. March, Ll.M. Mir, T. Medcalf, I.S. Quazi, J.A. Strong, L.R. West

Department of Physics, Royal Holloway & Bedford New College, University of London, Surrey TW20 OEX, United Kingdom[10]

D.R. Botterill, R.W. Clifft, T.R. Edgecock, M. Edwards, S.M. Fisher, T.J. Jones, P.R. Norton, D.P. Salmon, J.C. Thompson

Particle Physics Dept., Rutherford Appleton Laboratory, Chilton, Didcot, Oxon OX11 OQX, United Kingdom[10]

B. Bloch-Devaux, P. Colas, H. Duarte, W. Kozanecki, E. Lançon, M.C. Lemaire, E. Locci, P. Perez, F. Perrier, J. Rander, J.-F. Renardy, A. Rosowsky, A. Roussarie, J.-P. Schuller, J. Schwindling, D. Si Mohand, B. Vallage

Service de Physique des Particules, DAPNIA, CE-Saclay, 91191 Gif-sur-Yvette Cedex, France[17]

R.P. Johnson, A.M. Litke, G. Taylor, J. Wear

Institute for Particle Physics, University of California at Santa Cruz, Santa Cruz, CA 95064, USA[27]

J.G. Ashman, W. Babbage, C.N. Booth, C. Buttar, R.E. Carney, S. Cartwright, F. Combley, F. Hatfield, L.F. Thompson[1]

Department of Physics, University of Sheffield, Sheffield S3 7RH, United Kingdom[10]

E. Barberio, A. Böhrer, S. Brandt, G. Cowan, C. Grupen, G. Lutters, F. Rivera,[32] U. Schäfer

Fachbereich Physik, Universität Siegen, 5900 Siegen, Fed. Rep. of Germany[16]

R. Della Marina, G. Giannini, B. Gobbo, F. Ragusa[21]

Dipartimento di Fisica, Università di Trieste e INFN Sezione di Trieste, 34127 Trieste, Italy

L. Bellantoni, W. Chen, D. Cinabro,[26] J.S. Conway,[30] D.F. Cowen,[20] Z. Feng, D.P.S. Ferguson, Y.S. Gao, J. Grahl, J.L. Harton, R.C. Jared,[6] B.W. LeClaire, C. Lishka, Y.B. Pan, J.R. Pater, Y. Saadi, M. Schmitt, V. Sharma, Z.H. Shi, A.M. Walsh, F.V. Weber, Sau Lan Wu, X. Wu, M. Zheng, G. Zobernig

Department of Physics, University of Wisconsin, Madison, WI 53706, USA[11]

---

†Deceased.

[1]Now at CERN, PPE Division, 1211 Geneva 23, Switzerland.

[2]Permanent address: University of Washington, Seattle, WA 98195, USA.

[3]Now at University of California, Irvine, CA 92717, USA.

[4]Also Istituto di Fisica Generale, Università di Torino, Torino, Italy.

[5]Also Istituto di Cosmo-Geofisica del C.N.R., Torino, Italy.

[6]Permanent address: LBL, Berkeley, CA 94720, USA.

[7]Supported by CICYT, Spain.

[8]Supported by the National Science Foundation of China.

[9]Supported by the Danish Natural Science Research Council.

[10]Supported by the UK Science and Engineering Research Council.

[11]Supported by the US Department of Energy, contract DE-AC02-76ER00881.

[12]Supported by the US Department of Energy, contract DE-FG05-87ER40319.

[13]Supported by the NSF, contract PHY-8451274.

[14]Supported by the US Department of Energy, contract DE-FC0S-85ER250000.

[15]Supported by SLOAN fellowship, contract BR 2703.

[16]Supported by the Bundesministerium für Forschung und Technologie, Fed. Rep. of Germany.

[17]Supported by the Direction des Sciences de la Matière, C.E.A.

[18]Supported by Fonds zur Förderung der wissenschaftlichen Forschung, Austria.

[19]Supported by the Korean Science and Engineering Foundation and Ministry of Education.

[20]Now at California Institute of Technology, Pasadena, CA 91125, USA.

[21]Now at Dipartimento di Fisica, Università di Milano, Milano, Italy.

[22]Also at CERN, PPE Division, 1211 Geneva 23, Switzerland.

[23]Now at DESY, Hamburg, Germany.

[24]Now at TRIUMF, Vancouver, B.C., Canada.

[25]Also at Università di Napoli, Dipartimento di Scienze Fisiche, Napoli, Italy.

[26]Now at Harvard University, Cambridge, MA 02138, U.S.A.

[27]Supported by the US Department of Energy, grant DE-FG03-92ER40689.

[28]Now at Università di Pavia, Pavia, Italy.

[29]Now at Max-Planck-Institut f. Kernphysik, Heidelberg, Germany.

[30]Now at Rutgers University, Piscataway, NJ 08854, USA.

[31]Now at Oxford University, Oxford OX1 3RH, U.K.

[32]Partially supported by Colciencias, Colombia.

1 Introduction

The polarisation of the taus observed at LEP results from parity violation in Z production and decay. The LEP beams are unpolarised and the inequality of the Z couplings to left-handed and right-handed leptons induces a polarisation of the taus as well as a polarisation of the Z. The polarisation of the Z induces a dependence of the polarisation of the taus on the angle between the Z polarisation vector (along the beam) and the τ line of flight [1].

Ignoring $\mathcal{O}(m_\tau^2/\mathrm{M}_\mathrm{Z}^2)$ corrections, the τ^+ and τ^- have opposite helicity. Herein P_τ is defined as the polarisation of τ^-. The dependence of P_τ on the angle θ between the beam e^- and the τ^- appears, at the Z peak, in the improved Born approximation [1], as

$$P_\tau(\cos\theta) = -\frac{\mathcal{A}_\tau(1+\cos^2\theta) + \mathcal{A}_\mathrm{e}(2\cos\theta)}{(1+\cos^2\theta) + \mathcal{A}_\tau\mathcal{A}_\mathrm{e}(2\cos\theta)} \tag{1}$$

where

$$\mathcal{A}_l \equiv 2g_V^l g_A^l/[(g_V^l)^2 + (g_A^l)^2], \tag{2}$$

and g_V^l and g_A^l are the vector and axial vector couplings of the Z to lepton l.

The measurement of P_τ as a function of $\cos\theta$ provides nearly independent determinations of $\mathcal{A}_\tau$ and $\mathcal{A}_\mathrm{e}$, testing the universality of the couplings of the Z to electrons and taus. The polarisation averaged over $\cos\theta$ is $-\mathcal{A}_\tau$, and $\mathcal{A}_\mathrm{e}$ is related to the forward-backward polarisation asymmetry by $\mathcal{A}_\mathrm{e} = -\frac{4}{3}\mathcal{A}_{FB}^{\mathrm{pol}}$. The correlation between the tau polarisation measurement and the forward-backward charge asymmetry is small enough to be ignored.

In the standard model, the lepton couplings are equal, and hence $\mathcal{A}_\tau = \mathcal{A}_\mathrm{e}$. Combining the measurements provides a more precise determination for $g_V^{\mathrm{e}-\tau}/g_A^{\mathrm{e}-\tau}$ and for the effective weak mixing angle through $g_V^l/g_A^l \equiv 1 - 4\sin^2\theta_W^{\mathrm{eff}}$.

The analysis of tau polarisation described in this paper improves upon the earlier analysis published by the ALEPH collaboration [2] in which only the averaged polarisation was measured. Better techniques of identification have also been employed. The results presented here, based on 18.8 pb^{-1} of data recorded during 1990 and 1991, supersede the earlier results, with which they are fully compatible. Particular attention has been paid to reducing systematic uncertainties from particle identification and contaminations. Checking the methods of identification and acceptances relies upon ALEPH data samples and test beam data.

The two methods used in this analysis, based respectively on individual tau decays and angular correlations, are first described. Then the common particle identification techniques are discussed. The decay channel selection and polarisation extraction procedures, the systematic error determination and the results are, for clarity, presented independently for the two methods, then the conclusions are drawn.

2 Method

The $V-A$ structure of the weak charged current, taken as exact in this analysis, makes the tau decays powerful analysers of the tau polarisation. In this analysis two methods are used. In the first, referred to below as the "single-tau method," one infers the polarisation from the kinematic distributions of single tau decays. Since the helicities of the two taus from a Z decay are opposite, each tau can be used independently. However one must take

into account their correlation when calculating the statistical error. Using the correlations between the kinematic quantities used in the single-tau method for both tau decays brings very little additional sensitivity. In the second method, referred to as the "acollinearity method," the polarisation is inferred from the angular correlation of the decay products of the two taus in an event.

The analysis described in this paper employs the tau decay modes $e\nu\overline{\nu}$, $\mu\nu\overline{\nu}$, $\pi\nu$, $\rho\nu$, and $a_1\nu$, together constituting more than 80% of all tau decays. Charged pions are not distinguished from kaons in the data. The decay modes $\tau \to \pi\nu$ and $\tau \to K\nu$ are treated together and referred to herein as "$\pi\nu$." Similarly, the final state $K\pi^0\nu$ falls into the "$\rho\nu$" channel. However, it is considered as background in the rho channel when calculating the selection efficiency and extracting the polarisation. A systematic error is assigned to account for the uncertainty in the corresponding branching ratio. In the a_1 case only the decay mode to three charged pions is used, and the decays to $K\pi\pi\nu$ and $K\overline{K}\pi\nu$ are treated as background.

The analysis selects tau candidates by retaining low-multiplicity events coming mainly from lepton-pair decays of the Z. After association of the charged particles and photons with one of the two hemispheres in the event, as defined by the event thrust axis, the identity of the charged particles and the presence of photons and/or π^0s determine the tau decay classification. Removal of non-tau background based on the kinematics of the opposite hemisphere largely avoids kinematic biases and loss of sensitivity, except for the energy correlations between hemispheres.

2.1 Single-tau Method

In the single-tau method the tau polarisation is extracted from the observed kinematic distributions by finding the admixture of left- and right-handed Monte Carlo taus which reproduces optimally the observed distributions.[1] A full Monte Carlo simulation of the detector response for tau and non-tau background events takes into account initial-state, final-state, and decay radiative corrections [1,3], detector acceptance and resolution.

For the lepton and pion decays, only one measurable energy exists. Defining $x = E_{\text{charged}}/E_{\text{beam}}$ the expected distributions [4], ignoring mass and radiative effects, depend linearly on a given longitudinal polarisation P_τ as

$$W(x_{\text{lept}}) = \frac{1}{3}\left[(5 - 9x_{\text{lept}}^2 + 4x_{\text{lept}}^3) + P_\tau(1 - 9x_{\text{lept}}^2 + 8x_{\text{lept}}^3)\right] \tag{3}$$

and

$$W(x_\pi) = 1 + P_\tau(2x_\pi - 1). \tag{4}$$

In the case of the multipion decays, the distribution has the same general expression:

$$W(\vec{\xi}) = a(\vec{\xi}) + P_\tau b(\vec{\xi}) \tag{5}$$

where $\vec{\xi}$ is the set of observed momenta. It can be recast in a form similar to the pion distribution [5]:

$$W(\omega) = f(\omega)(1 + P_\tau\omega) \tag{6}$$

[1] Since in this analysis one does not observe the azimuthal dependence of the decays it is possible to assign a helicity to each Monte Carlo event.

by using the quantity $\omega(\vec{\xi})$, defined by

$$\omega(\vec{\xi}) = \frac{b(\vec{\xi})}{a(\vec{\xi})} = \frac{W_+(\vec{\xi}) - W_-(\vec{\xi})}{W_+(\vec{\xi}) + W_-(\vec{\xi})}, \tag{7}$$

where W_+ (W_-) is the probability density of $\vec{\xi}$ for positive (negative) helicity. Hence the variable ω expresses the normalized difference between the probability densities of the tau decay having originated from a positive or negative helicity tau. This quantity summarizes all available information about the helicity of a given tau decay and the use of the one-dimensional distribution of equation 6 yields an optimal determination of P_τ. This method applies as well to the lepton and pion cases, but is equivalent to simply using the energy.

Both the ρ and a_1 modes are treated using the ω variable. In the case of the ρ this takes fully into account the influence of the tau helicity state on the distributions of tau and rho decay angles, ψ_τ and ψ_ρ, respectively, as well as the effect of the $\pi^\pm\pi^0$ mass. In the case of the a_1 there are six quantities which describe the tau decay: two angles ψ_τ and ψ_a defined by the normal to the a_1 decay plane, the hadronic mass, the masses of the two $\pi^+\pi^-$ combinations in the a_1 decay, and the angle of one of the pions in the decay plane. The distribution of the angles ψ_τ and ψ_a does not depend on the hadronic matrix element. Previous analyses took only these two variables into account. Using the six quantities through the ω variable allows a significant improvement in the statistical sensitivity for the a_1 channel: it becomes more sensitive than either of the leptonic decay modes. An expanded discussion of ω for the $\rho\nu$ and $a_1\nu$ decay channels appears in appendix A.

The tau polarisation has a weak dependence on centre-of-mass energy. The distribution of recorded luminosity is almost equal above and below the resonance and the effect on the polarisation nearly cancels out when making the average. Therefore this effect is ignored in the analysis and the average polarisation over the different centre-of-mass energies is determined. Then a small correction is applied to the result to account for this and small radiative effects. These corrections affect $\mathcal{A}_\tau$ and $\mathcal{A}_e$ in an essentially identical way. To avoid confusion the measured quantities before correction will be written A_τ, A_e, and $A_{e-\tau}$, whereas the calligraphic symbols $\mathcal{A}_\tau$, $\mathcal{A}_e$, and $\mathcal{A}_{e-\tau}$ will be reserved for the physical quantities with corrections. In order that the kinematics of the simulated events match those of the data the distribution in centre-of-mass energy of the Monte Carlo matches that for the data.

2.2 Acollinearity Method

One can also extract the polarisation from the acollinearity distribution of the decay products of the two taus in one event[6]. In this method the polarisation is determined by fitting a tree-level theoretical prediction for the acollinearity, with no initial- or final-state radiation, to the observed distribution. The selected events have both taus decaying to final states with a single charged track, and the distributions are corrected for acceptance and radiative effects. The acollinearity is defined using charged tracks only, as $\varepsilon = \pi - \theta_{12}$, where θ_{12} is the opening angle between the tracks.

The acollinearity distribution, for a given $\cos\theta$, may be written

$$\frac{1}{\sigma}\frac{d\sigma}{d\varepsilon} = W(\varepsilon) = F(\varepsilon) + P_\tau(\cos\theta)\ G(\varepsilon), \tag{8}$$

where functions F and G reflect the kinematics of the particular tau decay channels and are described in appendix B.

The parameters $\mathcal{A}_\tau$ and $\mathcal{A}_e$ can be extracted from the acollinearity distribution integrated over $\cos\theta$ and the forward-backward asymmetry as a function of acollinearity, which at $s = M_Z^2$ are given by [6]:

$$\frac{1}{\sigma}\frac{d\sigma}{d\varepsilon} = F(\varepsilon) - \mathcal{A}_\tau G(\varepsilon) \tag{9}$$

$$A_{FB}(\varepsilon) = \frac{3}{4}\mathcal{A}_e \frac{F(\varepsilon)\mathcal{A}_\tau - G(\varepsilon)}{F(\varepsilon) - G(\varepsilon)\mathcal{A}_\tau}. \tag{10}$$

A fit using equation 10, however, implicitly uses the information from the normalization of $A_{FB}(\varepsilon)$, i.e. the forward-backward charge asymmetry A_{FB}. Since the information on A_{FB} is already used with the lineshape fits [7], an alternative set of observables, $d\sigma^F/d\epsilon$ and $d\sigma^B/d\epsilon$, is defined by separately integrating the acollinearity distribution (equation 8) over the forward ($\cos\theta > 0$) and backward ($\cos\theta < 0$) hemispheres, respectively. Then $\mathcal{A}_\tau$ and $\mathcal{A}_e$ are derived from the measured values of P_τ in the two hemispheres.

The kinematics of the decay products of a single tau and the acollinearity of the two taus are correlated, and hence so are the extracted polarisations. The systematic uncertainties in measuring angles are, however, largely independent of the systematics in the single-tau method.

3 ALEPH Detector and Data

The ALEPH detector is described in detail elsewhere [8]; the main elements used in this analysis include

- the inner tracking chamber (ITC), a cylindrical eight-layer axial-wire drift chamber, extending from 13 to 29 cm radius,
- the time projection chamber (TPC), extending to 1.8 m in radius, which, combined with the ITC, provides momentum resolution of $\delta p/p^2 = 8\times10^{-4}\mathrm{GeV}^{-1}$, and with up to 330 samples of specific ionization a measurement of dE/dx with 4.6% resolution,
- the electromagnetic calorimeter (ECAL), a lead sheet/wire chamber sandwich of 45 layers with a fine-grained (16×16 mrad) projective-tower cathode pad readout segmented in three "stacks" of 4, 9, and 9 radiation lengths in depth, having an energy resolution of $18.7\%/\sqrt{E} \oplus 2.1\%$, and with an independent low-noise readout of each of the 45 sense wire planes in a module,
- the hadronic calorimeter (HCAL), consisting of 23 layers of streamer tubes interleaved in the magnet iron return yoke, with the individual tube hits recorded digitally and a projective tower cathode pad readout of hadronic energy, and
- the muon chambers, two double layers of streamer tubes with orthogonal strips surrounding the HCAL, providing two three-dimensional coordinates for muons which pass through the HCAL.

1990		1991	
energy (GeV)	integrated luminosity (pb^{-1})	energy (GeV)	integrated luminosity (pb^{-1})
88.22	0.482	88.46	0.668
89.22	0.520	89.46	0.797
90.22	0.447	90.21	0.753
91.22	3.624	91.23	7.546
92.21	0.555	91.95	0.693
93.21	0.597	92.95	0.677
94.20	0.642	93.70	0.768

Table 1: Integrated luminosity collected at each energy point.

The ITC, TPC and ECAL all lie inside the superconducting solenoid, which provides a 1.5 Tesla magnetic field.

The study of tau decays benefits from the main features of the detector: three-dimensional track separation in the TPC, high granularity of the electromagnetic calorimeter, and the HCAL digital pattern. The acollinearity resolution in two-track events is about 1.5 mrad.

This analysis employs data recorded by ALEPH in 1990 and 1991, representing a total of over 20,000 observed tau pair events. Only data collected in which all the detectors listed above were operational are considered. The data were recorded at centre-of-mass energies at and near the Z mass. Table 1 lists the integrated luminosity at each energy point. The single-tau method for measuring the polarisation employs data from all LEP energies. The acollinearity method is restricted to data collected at the Z peak.

4 Particle Identification

Classification of the decay modes of the tau relies on the presence, identity, and kinematics of charged tracks, photons and π^0s. This section discusses the tools for measuring charged particle momenta, determining the identity of charged particles, and reconstructing photons and π^0s. The performance of these tools has been checked extensively not only using Monte Carlo simulation but as much as possible using physics channels well identified in the data like Z decays into muon or electron pairs, or $\gamma\gamma$ interactions.

4.1 Charged Particles

The tracking detectors (ITC and TPC) measure a three-dimensional trajectory for each charged particle ("track"), and in addition the TPC provides a measurement of the relative ionization of a charged particle. Charged particles deposit energy in the calorimeters, ECAL and HCAL, and possibly leave hits in the muon chambers. Based on this information the analysis employs two methods for determining the charged particle identity. In one, referred to as the "classical cut" or "CC" method, one identifies particles by placing cuts on the values of the associated variables. The other method employs a neural network using simultaneously the information from the tracking and calorimetry, and is referred to

as "NN." In the NN method each particle receives a unique assignment, whereas for the CC method the assignment for the electrons depends on the decay channel being analysed.

TPC dE/dx

The TPC can resolve tracks from particles separated by typically 2 cm or more for 25 cm of their trajectory. Given the dE/dx, track momentum, and particle mass hypothesis, the signed number of standard deviations $R_{dE/dx}$ by which the measured dE/dx differs from the prediction can be calculated and used as a discriminating variable.

ECAL Estimators

Two estimators, called R_{L} and R_{T} [8], give the number of standard deviations by which the observed electromagnetic energy deposit differs in longitudinal and transverse shape, respectively, from that expected from an electron with a given momentum. More precisely R_{T} measures the amount of energy in the shower core compared to the track momentum.

HCAL, Muon Chamber Information

To improve the muon-pion-electron separation, a pattern recognition algorithm which makes use of the digital pattern of the hit calorimeter tubes has been developed. This pattern is significantly different for muons, pions, and electrons reaching the HCAL, but suffers from dead zones and inefficiencies. The main aim of the algorithm is to overcome these problems. It proceeds by connecting hit tubes, building an outgoing "tree" structure which can be associated to charged tracks. The result of this operation is summarized in a number of variables which describe the trees by themselves, such as their length, energy or level of ramification, as well as by their relationships to tracks, such as distance or angle.

Charged Particle Identification Using Cuts

Using the various estimators described above one can identify tracks by requiring the values of the estimators to lie in certain ranges. The cut method employed in this analysis begins by identifying electrons and muons.

Two sets of electron identification criteria are defined and used according to the physics goal. The first selects electrons for the analysis of the electron channel, emphasizing the quality of the energy measurement in the calorimeter. The second provides a veto against electrons with a reduced loss of pions.

For selecting muons, due to the inhomogeneity of the HCAL, the cut criteria must take into account the differences of the various regions of the detector. The criteria used to define the muon sample can be summarized in the following way: either the track penetrates through to the muon chambers with a dispersion compatible with the multiple scattering, or the HCAL tree associated is long, straight and not ramified, and close to the extrapolated track.

Any track not selected by these requirements is not kept as a muon.

Any track not identified as an electron by the second set of criteria or as a muon is classified as a pion. Table 2 summarizes the performance of the method on Monte Carlo events.

track ID	Sources of Monte Carlo particles				
	$\tau \to e\nu\bar{\nu}$	$\tau \to \mu\nu\bar{\nu}$	$\tau \to \pi\nu$	$Z \to e^+e^-$	$Z \to \mu^+\mu^-$
e for $e\nu\bar{\nu}$	**96.1±0.1**	-	0.6±0.1	**95.3±0.2**	-
e for $\pi\nu$	**97.3±0.1**	-	0.3±0.1	**96.3±0.2**	-
μ	-	**99.6±0.1**	1.7±0.1	-	**99.4±0.1**
π	2.7±0.1	0.4±0.1	**98.0±0.1**	3.7±0.2	0.6±0.1

Table 2: Efficiency (in percent) for conventional cut particle identification method, for Monte Carlo tracks with p/E_{beam} above 0.05 and $|\cos\theta| < 0.9$. The calorimeter cracks are not taken into account for the electron and pion efficiencies. They induce a 4% additional loss in acceptance. The two rows for the electron identification correspond to the fact that the procedure differs when it is used for the analysis of the electron or of the pion channel. The three last lines add to 100%.

track ID	Sources of Monte Carlo particles				
	$\tau \to e\nu\bar{\nu}$	$\tau \to \mu\nu\bar{\nu}$	$\tau \to \pi\nu$	$Z \to e^+e^-$	$Z \to \mu^+\mu^-$
e	**98.9±0.1**	-	1.4±0.1	**98.4±0.1**	-
μ	-	**99.2±0.1**	1.2±0.1	-	**99.5±0.1**
π	1.1±0.1	0.8±0.1	**97.4±0.1**	1.6±0.1	0.5±0.1

Table 3: Efficiency (in percent) for neural network particle identification method, for tracks with p/E_{beam} above 0.05 and $|\cos\theta| < 0.9$ from Monte Carlo lepton pair events. The fiducial region includes the cracks between calorimeter modules.

Charged Particle Identification using a Neural Network

A different approach to classify charged particles as electrons, muons, or pions (hadrons, in general), uses information from the TPC, ECAL, HCAL tree quantities, and muon chambers simultaneously in an artificial neural network [9]. Twenty quantities associated with each charged track in an event form the input to a feed-forward perceptron type neural network which has two hidden layers of ten nodes each, and three outputs designated as electron, muon, and pion. The twenty quantities include the track momentum, polar angle, azimuthal angle, electron and pion dE/dx estimators, total and individual layer ECAL cluster energies, eight HCAL tree quantities, and estimators from muon chamber hits. The network training employs a sample of 18600 electrons, 10700 muons, and 26000 pions from Monte Carlo lepton-pair events, mainly tau pairs. Each track in the training sample is presented an average of about 2000 times during the network training. Table 3 shows the resulting performance for tracks from Monte Carlo lepton pair events. The neural net identifies each charged particle as either e, μ, or π, regardless of the channel classification applied later.

4.2 Photons and π^0s

The photon reconstruction makes use of the three-dimensional segmentation of the ECAL. A reconstructed photon appears as a cluster of storeys, where "storey" designates one of

the three depth segments of an ECAL projective tower, that have an energy above a given threshold and whose distance from a charged track exceeds 2 cm. The algorithm looks for local energy maxima: storeys which have more energy than the ones they share a face with, their "neighbours." Every storey which is not a local maximum is assigned to the cluster of its neighbour of maximal energy. The energy of the photon is then computed from the energy of the four central towers, applying a polar angle dependent correction factor averaging about 1.15. The photon direction is calculated from the barycenter of the cluster.

Photons which convert in the detector material are reconstructed from pairs of oppositely charged tracks, identified as electrons, emanating from the same point, with invariant mass close to zero.

In the tau physics environment, photon reconstruction must efficiently reject fake photons, separate photons from charged tracks, and reconstruct overlapping photon pairs. Fake photons may appear because a charged track has produced small "satellite" clusters from shower fluctuations. In order to reject such fake photons, the energy of the candidate must exceed 300 MeV, contain energy in at least two consecutive stacks, and have a ratio of the sum of energies in the first two stacks to the total higher than 70%.

The identification of π^0s is very important in the separation of several τ decay channels, for instance π, $\rho \rightarrow \pi\pi^0$ and $a_1 \rightarrow \pi\pi^0\pi^0$. The $\gamma\gamma$ mass distribution of selected tau events with two photon candidates, shown in figure 1, has a clear peak at the π^0 mass. Nevertheless at low energies one of the two photons can be lost due to the energy threshold, and as the π^0 energy increases the photons become difficult to resolve and may be reconstructed as a single photon. This is illustrated using a sample of rho decay candidates, as defined in section 5.1. The upper plot of figure 2 shows the fraction of rho candidates where the π^0 is reconstructed as a single photon, as a function of the π^0 energy.

A check of the assertion that the high-energy single-photon π^0 candidates are in fact π^0s relies on a technique developed to resolve further the two photons not separated by the technique of local maxima described above. By computing the moments of the energy distribution up to third order, one can determine whether the cluster actually results from two photons. The method retains efficiency up to 45 GeV. The technique has been applied to the photons in the rho candidates: both those separated photons which, combined, make π^0s, and the single-photon π^0 candidates. The moments algorithm finds that the photons in the first category are indeed single photons, and not themselves π^0s, and at medium energies is able to resolve the two photons in the second category. This is illustrated in the lower plot of figure 2 where the fraction of rho candidates with still only one photon found by the moments algorithm is plotted. This provides evidence that these single-photon π^0 candidates are indeed mostly π^0s. At low π^0 energies the behaviour is very similar to that of the upper plot, showing that one of the photons has indeed been lost.

5 Single-tau Method

5.1 Selection

Selection of a pure sample of tau decays proceeds in three stages. Firstly, a simple event selection rejects most Z decays to hadrons. Secondly, the individual tau decays are classi-

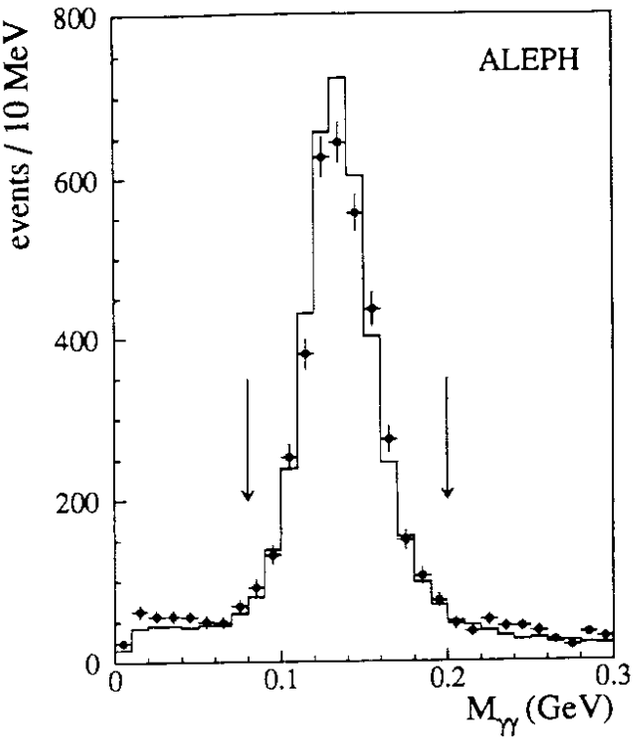

Figure 1: Comparison of real (points with error bars) and simulated (histogram) distributions of $\gamma\gamma$ masses. The arrows indicate the mass requirement for π^0s in the rho channel.

fied. Finally, requirements on the hemisphere opposite to the tau decay candidate greatly reduce non-tau backgrounds. The overall acceptance and contamination are given at the end of this section.

Most Z decays to hadrons are excluded by requiring fewer than nine tracks coming from the interaction region and that tracks have an angle less than 31.8 degrees with the axis of the jet. Poorly reconstructed events and two-photon events are excluded by demanding at least two charged tracks, and at least one track with momentum above 3 GeV. The thrust axis is calculated from the charged tracks, and the event divided into hemispheres. To avoid Bhabha background and poorly reconstructed tracks the thrust axis polar angle θ must satisfy $|\cos\theta| < 0.9$. This initial event selection retains 84% of the tau events produced, and 99% of those within the angular acceptance.

The identity of the charged tracks and the number of photons accompanying them distinguish each of the decay modes considered in this analysis:

- The presence of a single electron or muon track, with no or few photons, indicates $\tau \to e\nu\overline{\nu}$ and $\tau \to \mu\nu\overline{\nu}$ decays.

- A $\tau \to \pi\nu$ decay is identified by a single identified pion track with zero photons. This last requirement keeps backgrounds to a minimum without greatly sacrificing efficiency. The rho and electron backgrounds in the pion channel are reduced further by requiring low energy in the first four radiation lengths of the electromagnetic calorimeter.

- The rho channel is distinguished by a single charged track and evidence of photons from one, and only one, π^0; hemispheres with extra photons are rejected. A π^0

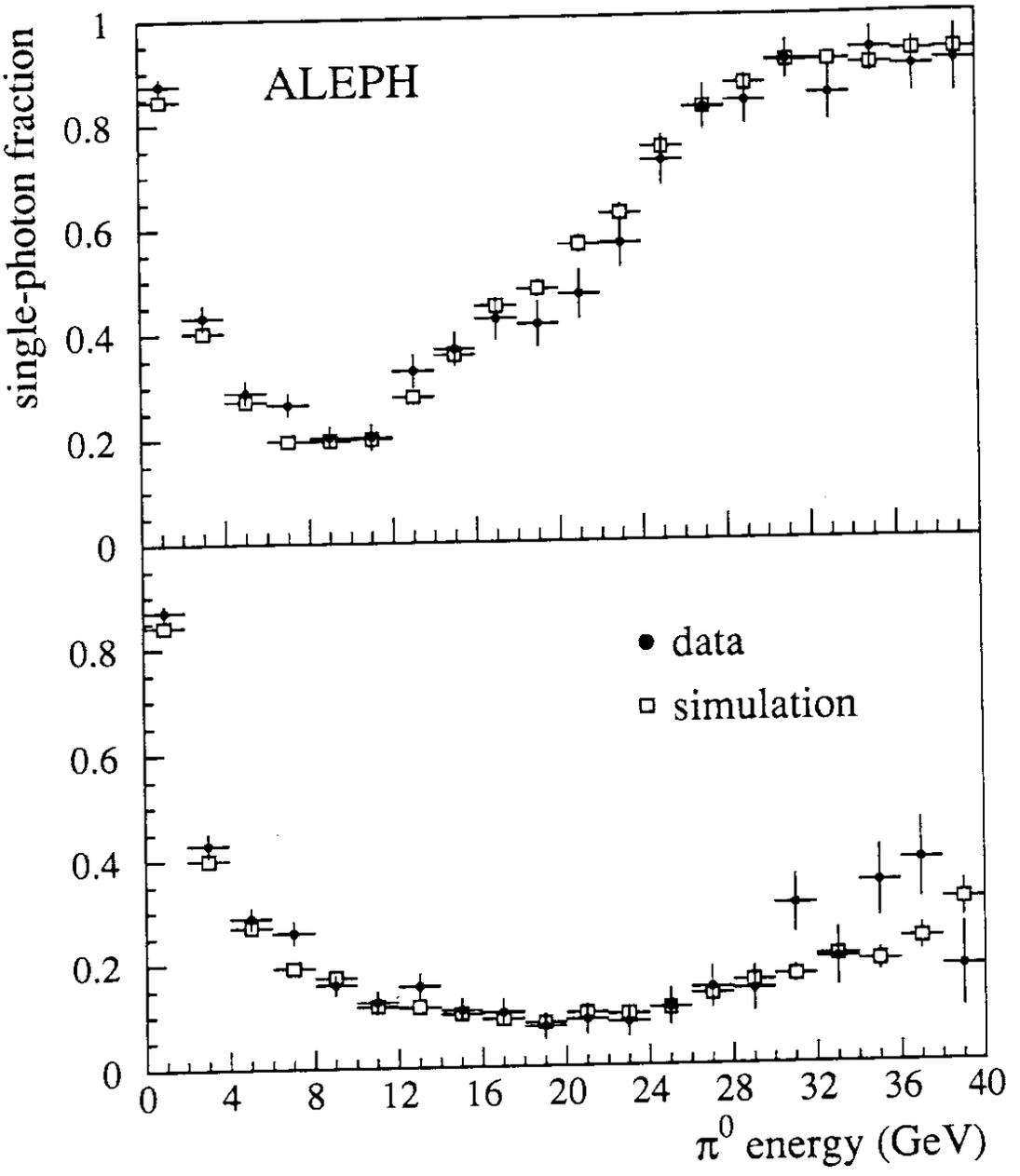

Figure 2: Fraction of rho candidates in which the π^0 is a "single photon" as a function of the π^0 energy. The upper plot shows this fraction as calculated from the reconstructed photons used in the polarisation analysis. The lower plot shows this fraction as calculated after a moments analysis has been performed on every reconstructed photon to check for the presence of a substructure originating from a π^0. At low energies the fraction of single photon π^0 candidates is the same indicating that one photon has indeed been lost. At high π^0 energy the two photons can merge in the calorimeter. The cut on minimum single-photon π^0 energy for the definition of rho candidates was removed for this figure.

candidate may be a pair of photons with invariant mass in the range 0.08 to 0.2 GeV, which is referred to as a "resolved" π^0. In decays with a resolved π^0 no particle identification is applied to the charged track. A π^0 candidate may also appear as a single photon, referred to as a "merged" π^0. Merged π^0s originate either from an energetic π^0 with the two photon showers overlapping, or from an asymmetric π^0 decay with one lost photon. To insure that the lost photon is the less energetic of the two, merged π^0s are required to have energy above 4 GeV. The charged track accompanying a merged π^0 must be identified as a pion. To be accepted as a $\tau \to \rho\nu$ decay the π^0 and charged track must have an invariant mass between 0.5 and 1.2 GeV. Figure 3 shows the comparison of the distribution of this mass for the selected sample with that of the simulation.

- To be selected as a three prong decay of the a_1 a hemisphere must contain three tracks, none of them identified as an electron, and no photons. As the a_1 decays predominantly into $\rho\pi$, demanding one $\pi^+\pi^-$ combination with an invariant mass consistent with that of the ρ suppresses background further. The observed and simulated three pion invariant mass distributions are compared in figure 4.

Given a candidate tau decay in one hemisphere, restrictions on the track type, angle, and energy of the recoil hemisphere reduce further contamination from non-tau events. This contamination comes from decays of the Z into electrons, muons, and hadrons, and from two-photon interactions.

- Electron channel candidates from two-electron events are excluded in order to reject Bhabha events from the sample of $\tau \to e\nu\overline{\nu}$ decays.

- Muon channel candidates from two-muon events are accepted only if the event visible energy is significantly less than the centre-of-mass energy. Contamination from $\gamma\gamma$ interactions is reduced by requiring a minimum total energy.

- Pion channel candidates suffer from Bhabha and muon pair background in which tracks are sometimes misidentified as pions. The resulting background must be reduced by rejecting candidates in which the recoiling hemisphere contains an electron or a muon, perhaps with radiated photons, with a large fraction of the beam energy.

- In the a_1 analysis referred to as CC, the non-tau background is rejected by applying an event selection [10] based on the event energy flow before the track identification.

Table 4 lists the performance characteristics for the two analyses. The analyses use the same approach to channel classification and background rejection. The absolute acceptance, defined with respect to the number of tau pairs produced, ranges from 40% in the $e\nu\overline{\nu}$ channel to 70% in the $\mu\nu\overline{\nu}$ channel, as illustrated in figure 5. The two methods give very similar performance in all channels except the electron channel, where in method NN the inclusion of the calorimeter crack and overlap regions and a lower minimum energy, provide additional acceptance. The acceptance and background fractions are estimated using a full simulation of the production of tau pairs and of the apparatus, but also are checked on selected data samples; this is described in the systematic uncertainties section. The fraction of candidate hemispheres which are incorrectly assigned is also shown in the

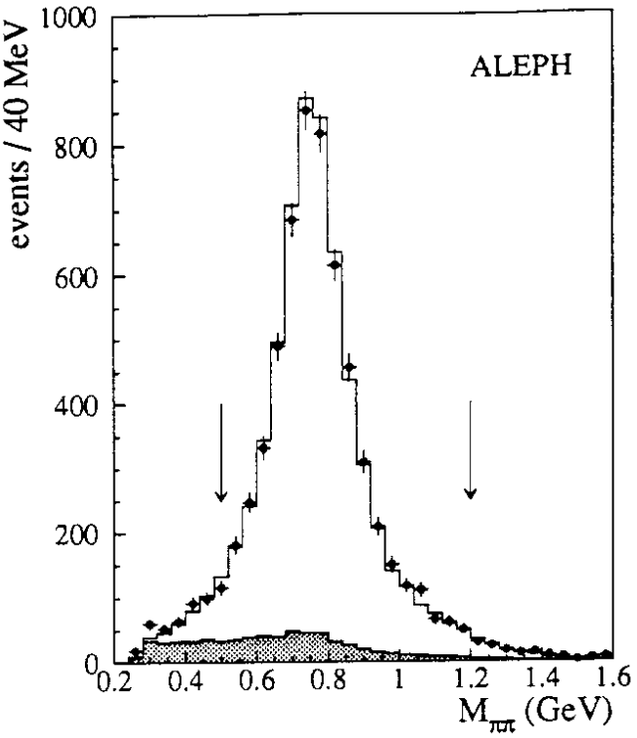

Figure 3: Comparison of the $\pi^{\pm}\pi^{0}$ mass distribution from rho candidates selected without the rho mass cut applied. Points with error bars show distribution of selected events, and histogram shows distribution from simulation; shaded histogram shows background. The arrows indicate the range of $\pi^{\pm}\pi^{0}$ mass allowed in the rho channel selection.

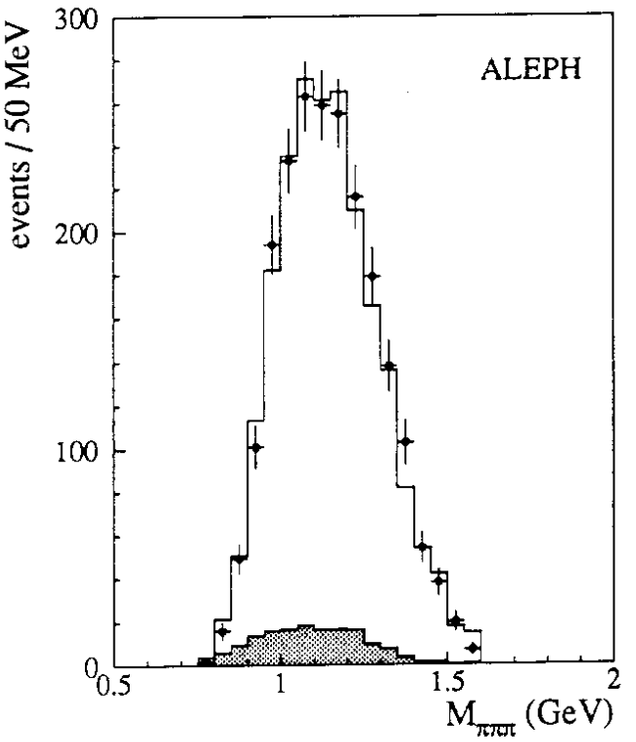

Figure 4: Comparison of the $\pi^{\pm}\pi^{+}\pi^{-}$ mass distribution from a_1 candidates. Points with error bars show the distribution of selected events, and the histogram shows the distribution from simulation; the shaded histogram shows the background.

item	decay channel				
	$e\nu\overline{\nu}$	$\mu\nu\overline{\nu}$	$\pi\nu$	$\rho\nu$	$a_1\nu$
method CC					
candidates	3019	5677	3287	5279	2147
acceptance (%)	40	69	61	48	55
tau background (%)	0.7	2.5	6.0	6.3	7.9
non-tau background (%)	1.0	2.3	0.5	0.4	0.0
method NN					
candidates	3780	5492	3438	5232	2153
acceptance (%)	48	70	61	47	53
tau background (%)	1.9	1.3	7.0	6.2	7.2
non-tau background (%)	1.1	1.1	1.5	0.6	0.0

Table 4: Performance of channel classification and background rejection.

table. The background levels are quite small, leading to correspondingly small systematic uncertainties.

5.2 Polarisation Extraction

Kinematic Quantities Employed

The distributions of ω and x depend linearly on P_τ. This allows extraction of the polarisation by comparing the observed distribution with a Monte Carlo distribution parametrised by the polarisation.

For the single-prong decay channels $e\nu\overline{\nu}$, $\mu\nu\overline{\nu}$, and $\pi\nu$ the variables x and ω are equivalent, and x is used. For the muon and pion cases the best estimate of the energy comes from the tracking detectors. In the case of the electron channel, however, the electron tends to lose energy due mainly to bremsstrahlung, leading to a systematic underestimation of E_e when using its momentum determination. To recover the energy otherwise lost one uses information on E_e provided by the electromagnetic calorimeter. This is done differently in the two single-tau analyses. In the NN method, the true electron energy is usually estimated as the sum of the energy in the calorimeter storeys. When the electron passes within 4.5 cm of a calorimeter crack its momentum plus the energy of all the photons reconstructed in the hemisphere is used. Method CC uses the sum of the calorimeter wire energy in all modules which contain a storey cluster in the relevant hemisphere. This necessitates eliminating electrons in cracks and overlap region between barrel and end caps, but provides an energy measurement insensitive to thresholds.

Polarisation from Single-tau Distributions

To extract the polarisation, a binned log likelihood relating observed and predicted kinematic distributions is maximised with respect to changes in the polarisation. The predicted number M_j^i of tau candidates classified in decay channel i ($i = e, \mu, \pi, \rho, a_1$) from

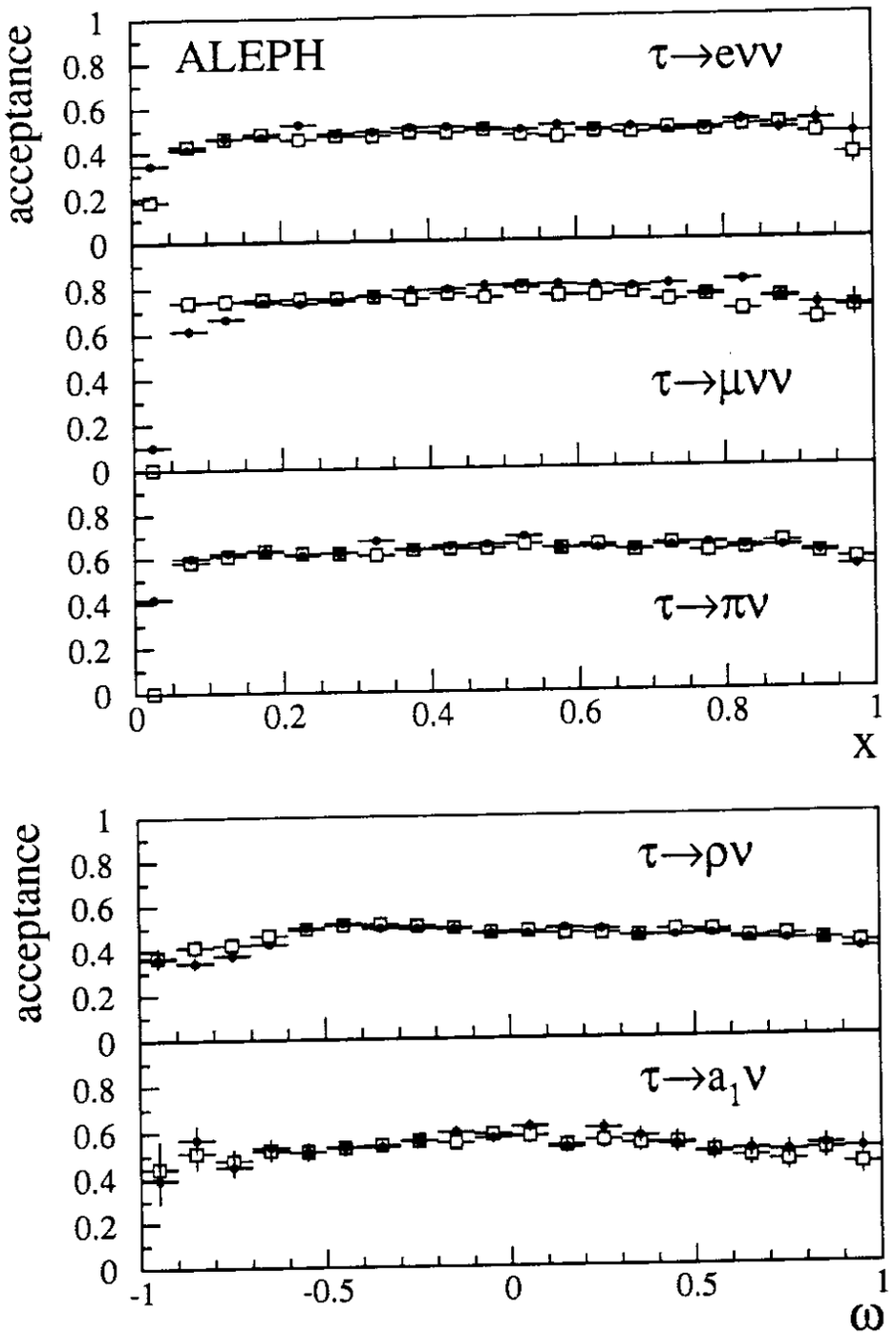

Figure 5: Absolute acceptance in each decay channel as a function of the variable used to extract the polarisation. The points represent the NN method, and the hollow squares represent the CC method.

Monte Carlo in a given bin j of ω (or x), is the sum

$$M_j^i = C_j^i + \sum_{l \neq i} W_j^{il} + \sum_k B_j^{ik}, \tag{11}$$

where C_j^i is the number of correctly identified tau decays in channel i, W_j^{il} is the number of taus incorrectly identified as coming from channel i but which in fact originated from some other decay mode l, and B_j^{ik} is non-tau background from source k ($k = e^+e^-, \mu^+\mu^-, \gamma\gamma \rightarrow$ leptons, $\gamma\gamma \rightarrow$ hadrons, $q\bar{q}$). All the dependence on tau polarisation P_τ is carried in C_j^i and W_j^{il}, which can be written

$$C_j^i = F^i(P_\tau)(N_{\rm gen}^{Ri} + N_{\rm gen}^{Li}) \left(\frac{(1+P_\tau)}{2} \cdot \frac{C_j^{Ri}}{N_{\rm gen}^{Ri}} + \frac{(1-P_\tau)}{2} \cdot \frac{C_j^{Li}}{N_{\rm gen}^{Li}} \right) \tag{12}$$

and similarly

$$W_j^{il} = F^l(P_\tau)(N_{\rm gen}^{Rl} + N_{\rm gen}^{Ll}) \left(\frac{(1+P_\tau)}{2} \cdot \frac{W_j^{Ril}}{N_{\rm gen}^{Rl}} + \frac{(1-P_\tau)}{2} \cdot \frac{W_j^{Lil}}{N_{\rm gen}^{Ll}} \right). \tag{13}$$

The superscripts R and L refer to the particular τ^- helicity. $N_{\rm gen}^{Rl}$ and $N_{\rm gen}^{Ll}$ give the number of decays generated by the Monte Carlo in channel l for each τ^- helicity. The factors F^i (or F^l) are such that the predicted number of taus in the Monte Carlo equals the total number of tau candidates in the data, minus the predicted non-tau background. The non-tau background is estimated by performing the selection procedure on Monte Carlo samples for the five non-tau background sources, normalized to the integrated luminosity.

Angular Dependence of Polarisation

The angular dependence of the polarisation is measured by extracting the polarisation in nine regions of polar angle. The relation 1 is then fitted to these data with A_τ and A_e as parameters. One can allow them to vary independently providing a test of universality. One can also constrain them to be the same $A_e = A_\tau \equiv A_{e-\tau}$ and fit for a single parameter. The correlation between A_τ and A_e is very small. The functional form of equation 1 is valid only at the Z peak, and does not include all radiative corrections. Thus the extracted values are corrected for these effects in the results section.

5.3 Systematic Uncertainties

The sources of systematic errors include acceptance, uncertainties in the background rate and theoretical uncertainties. The energy calibration and π^0 identification are important contributions as is the limited Monte Carlo statistical precision. The evaluation of these sources is discussed below. A summary of the errors in the single-tau method for each channel, common to both particle identification methods, appears in table 5.

The nature of the systematic uncertainties entering the $\mathcal{A}_\tau$ determination differ from those in $\mathcal{A}_e$ due to their dependence on electric charge and geometry. Most sources of systematic error tend to cancel for $\mathcal{A}_e$, as discussed below. Hence this discussion focuses on the systematic errors on $\mathcal{A}_\tau$.

Acceptance

Any imperfect modelling of the energy dependence of the efficiency for identifying charged particles, photons and π^0s can influence the measured polarisation by distorting the shape of the observed spectra. The ideal way to determine the level of this systematic uncertainty is to have a sample of particles in the detector with their identity known independently of the identification procedure used in the analysis. Comparison of the efficiency for this sample with that in the simulation leads in a straightforward way to a calculation of the apparent effect on polarisation.

For charged particles two types of data samples exist. In the first type, electrons, muons and pions from ALEPH data are identified without using any of the information upon which the particle identification is based. This rests mainly on physics channels which can be selected on a kinematical basis such as decays of the Z to electron or muon pairs, $\gamma\gamma$ interactions producing electron or muon pairs, photon conversions, τ decays with pions identified by the presence of a π^0 or two other charged pions. In the second type, test beam data with pions and electrons were collected using modules of the electromagnetic calorimeter. In both approaches one can infer the error induced on the polarisation from the momentum dependence of the ratio of the measured efficiency of the particle identification in the real data to that of the simulation. The test beam approach, used only for testing the ECAL part of the identification, has the advantage that the sample is manifestly unbiased and background-free, but requires a special simulation, represents only a particular polar angle in the detector and does not address the behaviour of the identification in or near cracks between calorimeter modules. Using particles from the kinematically identified channels overcomes these problems, but suffers somewhat from background and lack of statistics at momenta in the range 15-35 GeV.

For both types of leptons the precise measurement of particle identification efficiencies at high energy using $Z \rightarrow l^+l^-$ events and at low energy with $\gamma\gamma \rightarrow l^+l^-$ events and photon conversions, leads to a polarisation uncertainty of about 0.01. For pions, which are more sensitive to calorimeter modelling inaccuracies, both the test beam and kinematically identified pion samples indicate a polarisation shift of -0.006 ± 0.010, consistent with zero. The quoted systematic error represents the sum of the shift and its error.

For the a_1 channel particle identification enters in electron rejection. Assuming that the imperfections in the pion identification affect maximally the electron rejection, the study of the kinematically identified pion sample leads to an uncertainty in the polarisation of 0.014.

In the rho channel, the charged particle identification uncertainty plays a negligible role compared with that due to uncertainty in photon and π^0 reconstruction. Unfortunately the π^0 identification efficiency can not be checked with an independent sample of events; the only clean source of tagged π^0s is the rho events themselves. Nevertheless several tests using the data are possible.

One test of π^0 identification efficiency as a function of π^0 energy is to divide the sample of rhos into those with resolved and those with merged π^0s. The simulation reproduces well the observed fraction of rhos reconstructed from merged π^0s as can be seen in figure 2 (upper). The energy distribution of the two types of π^0 is correctly simulated and the polarisations measured with the two samples are consistent. The test beam data confirm that the Monte Carlo properly simulates electromagnetic showers as well as the quantities

used for charged pions in the analysis.

Another test is to vary the important cuts such as the low energy photon threshold, the minimum energy required for a merged π^0, and the π^0 and rho mass cuts. In all cases the change is consistent with the statistical fluctuation expected from events which are not common to the original and modified samples. An alternative photon finding algorithm with a looser definition of nearest neighbouring towers produces a discrepancy of 0.024 which is the largest discrepancy found and is taken as the systematic uncertainty for particle identification in the rho channel.

Since the π^0 acceptance depends on the π^0 energy, the acceptance as a function of the tau and rho decay angles is not symmetric. Dividing the sample into two parts, with $\cos\psi_\rho > 0$ and $\cos\psi_\rho < 0$, and extracting the polarisation in each, no discrepancy is apparent. More generally the agreement of the two-dimensional decay angle distributions shown in figure 7 is a check of the understanding of the acceptance. The same technique can be used for distributions of the a_1, shown in figure 8. For the a_1 the test could be done in the six-dimensional space but is plotted only for the two most commonly used variables.

Background

Uncertainties in the rate or distribution of background events, either from incorrectly identified tau decays or from non-tau sources, can lead to systematic uncertainty on the polarisation. The cross channel background from electron, muon or pion channels can be checked easily with the kinematically identified electrons, muons and pions. This can not be done, however, for the decays involving photons. If a photon is lost it is usually due to some well understood mechanism such as insensitive regions between ECAL modules, or energy below threshold, or impact within 2 cm of a charged track. Such effects are simulated in the Monte Carlo; the systematic error assigned comes from the change in polarisation calculated to result from a change in the background level of 20%.

The background in the rho and a_1 channels is located in phase space regions not crucial for the polarisation measurement, at intermediate values of the ω variable. To account for the large uncertainty in the $K\pi\pi$, $K\,\overline{K}\pi$, and $\pi\pi\pi\pi^0$ branching ratios, which produce background in the a_1 channel, those branching ratios have been varied by 50% in estimating the corresponding systematic error.

Energy Scale

In the leptonic decay modes of the tau, a major systematic error is due to uncertainty in the energy scale. The ECAL energy scale is set using electrons from Z decay and two-photon interactions. The uncertainty for the pad calibration is parametrised as a 0.3% scale error and $3\%/\sqrt{E}$ from imperfect pad clustering corrections. The wire calibration does not depend on this last effect but more on uncorrected inhomogeneities of the calorimeter response resulting in an equivalent systematic error. The TPC momentum scale is checked to be accurate to 0.2% using $Z \to \mu^+\mu^-$ events. The quoted systematic error results from the pessimistic assumption that this is an overall scale error rather than a sagitta error.

The energy scale errors have a small effect on the polarisation in the hadronic decay channels.

error	$e\nu\bar{\nu}$	$\mu\nu\bar{\nu}$	$\pi\nu$	$\rho\nu$	$a_1\nu$
acceptance	0.011	0.012	0.016	0.024	0.014
tau background	0.016	0.012	0.010	0.007	0.020
other background	0.012	0.008	0.002	0.003	-
energy calibration	0.032	0.014	0.001	0.012	0.001
model dependence	-	-	-	-	0.012
Monte Carlo statistics	0.021	0.017	0.008	0.010	0.020
total systematic error	0.045	0.029	0.018	0.030	0.034

Table 5: Summary of systematic errors on P_τ (and equivalently $\mathcal{A}_\tau$) for each decay channel, for the single-tau method.

Matrix Element Dependence in a_1

In the a_1 channel the definition of the variable ω is model dependent (see appendix A). Since the polarisation is measured by fitting the Monte Carlo distributions of ω to the experimental ones, an approximation in the definition of ω can modify the sensitivity of the measurement but does not bias it. Nevertheless, the fitting procedure is sensitive to the a_1 decay matrix element used in the Monte Carlo. The related systematic error is expected to be small [5]. The contribution of a 0^- state has been estimated to be negligible [5]. The possible existence of a ρ' component in the main $a_1 \to \rho\pi$ decay has also been taken into account in the systematic error. The error coming from the uncertainty on the possible fraction of D wave involved in the $a_1 \to \rho\pi$ [12,13] has been estimated by modifying the Monte Carlo matrix element through a reweighting procedure, and refitting the polarisation while keeping the same definition of ω taken from [11]. The maximal change of the result when the matrix element is varied within the limits determined by the ARGUS measurement [14] gives the corresponding systematic error.

Uncertainty in $\mathcal{A}_e$

The fact that $\mathcal{A}_e$ expresses the difference in polarisation in the forward and backward hemispheres leads to a low systematic error in its determination. Since "forward" and "backward" depend on the charge of the tau, only those systematic effects which show asymmetry in polar angle and charge enter as systematic effects on $\mathcal{A}_e$. In particular any systematic error which induces a shift in polarisation independent of $\cos\theta$ has almost no effect on $\mathcal{A}_e$. Different sources of systematic error on $\mathcal{A}_e$ have been investigated: residual uncorrected field distortions in the TPC volume which affect the tracks with $|\cos\theta| > 0.8$, acceptance, background, and the hadronic matrix element in the a_1 case. Their contributions to the systematic error on $\mathcal{A}_e$ are negligible, compared with the error from Monte Carlo statistics.

5.4 Single-tau Method Individual Channel Results

Table 6 shows the results of the fit for the polarisation in each of the individual channels, using both single-tau methods. The values of the polarisation in each channel agree within the expected statistical errors, taking into account the number of events in common. Com-

decay channel	method CC	method NN	difference	common fraction
$e\nu\overline{\nu}$	-0.179 ± 0.090	-0.294 ± 0.096	0.115 ± 0.074	0.68
$\mu\nu\overline{\nu}$	-0.142 ± 0.068	-0.163 ± 0.067	0.021 ± 0.036	0.86
$\pi\nu$	-0.133 ± 0.032	-0.132 ± 0.033	-0.001 ± 0.021	0.80
$\rho\nu$	-0.144 ± 0.031	-0.155 ± 0.031	0.011 ± 0.016	0.86
$a_1\nu$	-0.094 ± 0.066	-0.125 ± 0.064	0.031 ± 0.030	0.89

Table 6: Comparison of polarisation results from the two methods for each individual decay channel. The error is statistical only. The error quoted on the difference takes into account the average fraction of events in common for the two analyses.

decay channel	final result
$e\nu\overline{\nu}$	$-0.225 \pm 0.085 \pm 0.045$
$\mu\nu\overline{\nu}$	$-0.154 \pm 0.065 \pm 0.029$
$\pi\nu$	$-0.133 \pm 0.031 \pm 0.018$
$\rho\nu$	$-0.150 \pm 0.031 \pm 0.030$
$a_1\nu$	$-0.114 \pm 0.063 \pm 0.034$

Table 7: Combined individual channel polarisation results. The first error is statistical, the second contains all systematics including Monte Carlo statistics.

parison of the statistical and the systematic errors listed in table 5 shows that in none of the five channels is the measurement systematically limited. Figure 6 shows the fit results graphically for the five decay channels. Figure 7 shows the rho channel fit result displayed as a function of the tau and rho decay angles, and figure 8, the corresponding distributions for the a_1. Table 7 lists the combined results of the two methods, taking into account the events in common. The results for each decay mode show agreement with their common mean.

5.5 Single-tau Method Angular Fit Results

Figure 9 shows the data points entering the fit for the angular dependence of the polarisation. Table 8 shows the individual data points for both measurements, along with the combined result. For the single-tau method these values represent the least model-dependent way of presenting the results.

Table 9 lists the result of the fits for A_e, A_τ, and $A_{e-\tau}$ for the two single-tau methods. The results agree within the expectation, taking into account the roughly 80% sample overlap. The values of A_e and A_τ have a correlation coefficient from the fit of 0.024.

The systematic error on A_e is discussed above. The systematic error on A_τ is determined by averaging the single channel results assuming that the systematic errors from the channels are independent. The resulting uncertainty is 0.014. The systematic error on $A_{e-\tau}$ results from performing the angular fit assuming, in addition to the error on the

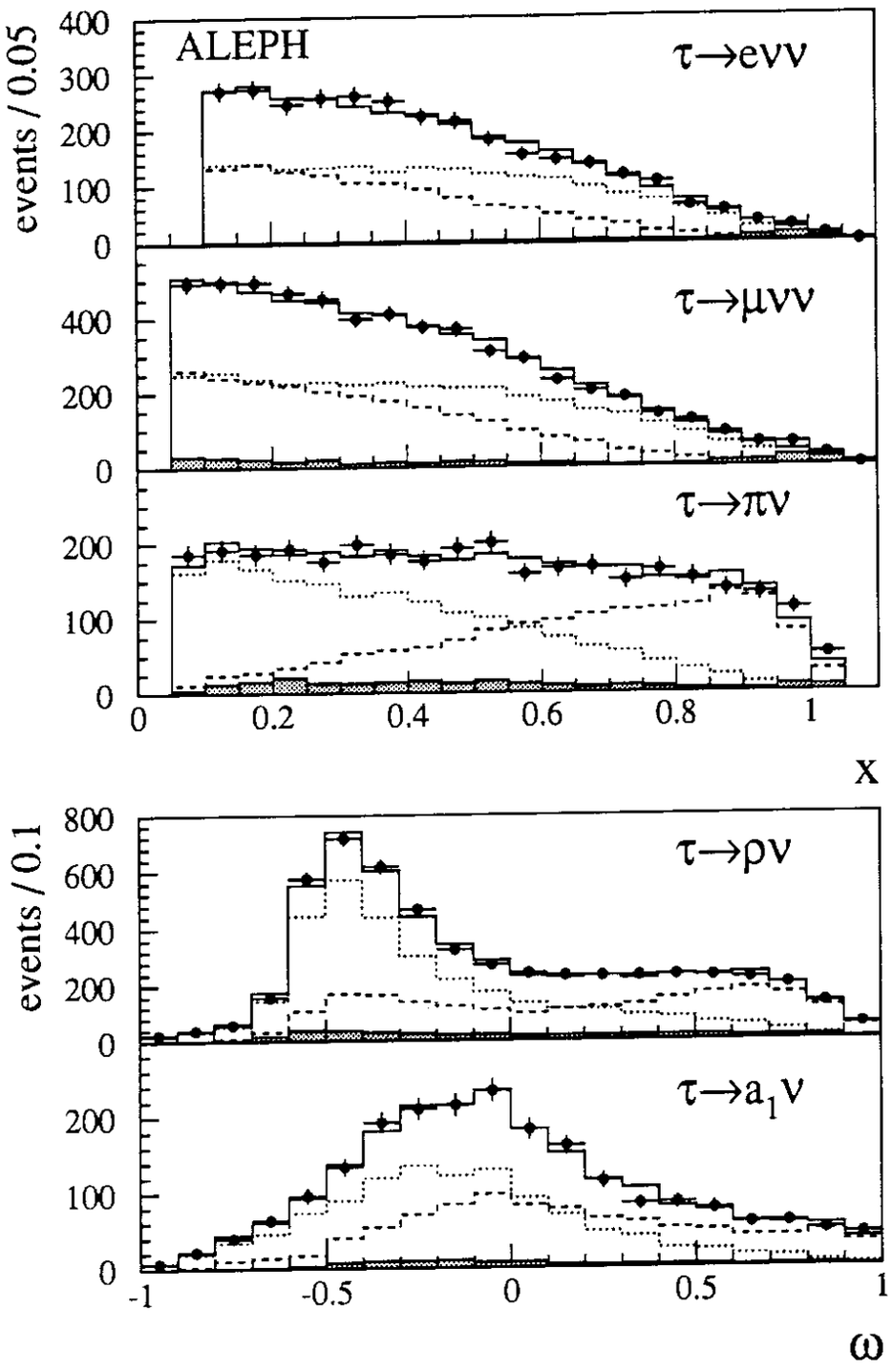

Figure 6: Fit results for the individual channels. The points with error bars are the observed spectra, the shaded histogram is the total background. The dashed (dotted) histogram is the Monte Carlo contribution from right- (left-) handed taus. The solid-line histogram indicates the sum of all Monte Carlo contributions.

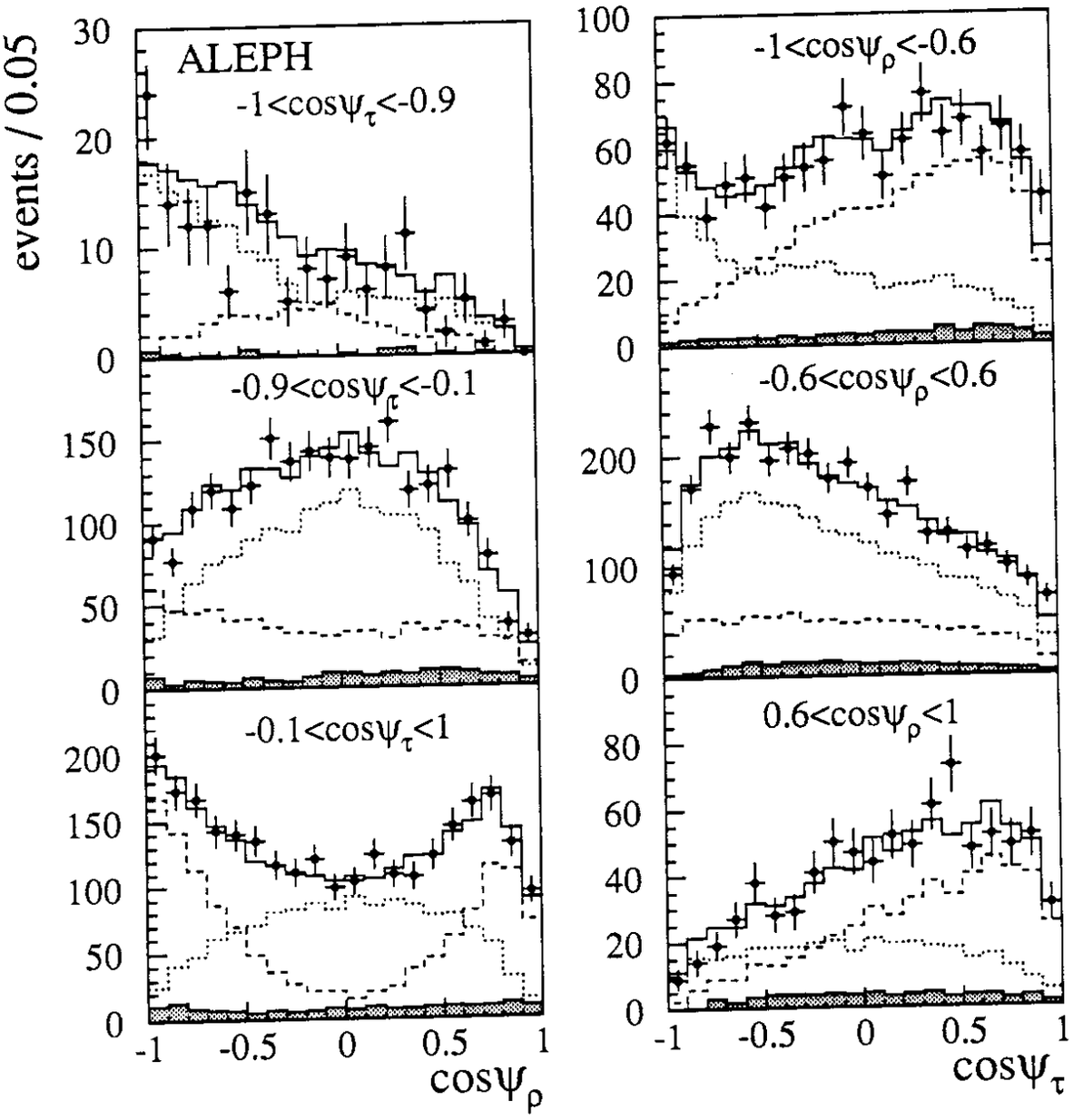

Figure 7: Rho channel fit result shown as projections in the tau and rho decay angles. The slices were chosen to bring out the distinctive features of the distribution. The dashed (dotted) histogram is the Monte Carlo contribution from right- (left-) handed taus. The solid-line histogram indicates the sum of all Monte Carlo contributions. The energy of the rho is simply related to $\cos\psi_\tau$. The energy difference between the pions from the rho decay is related to $\cos\psi_\rho$.

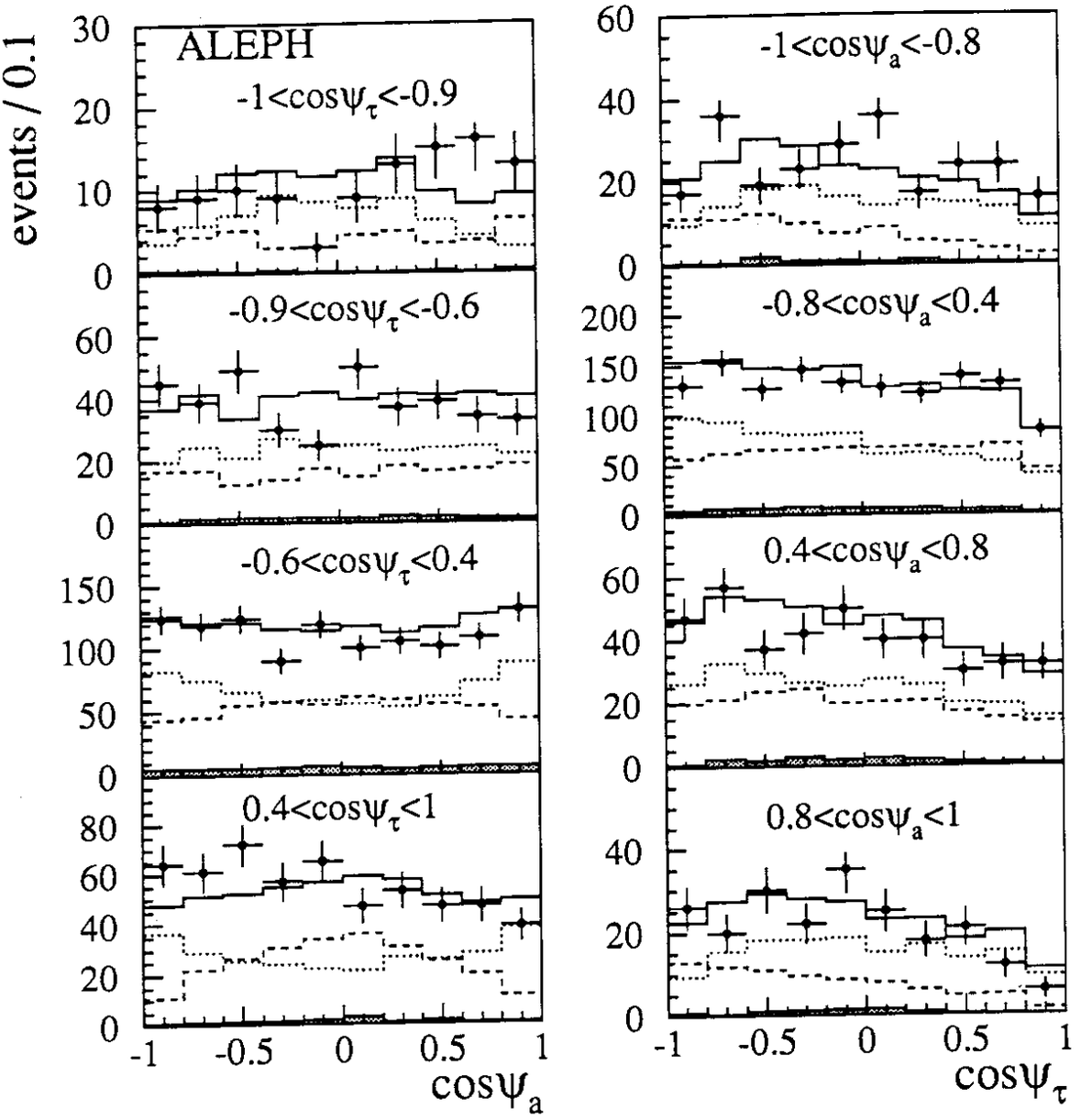

Figure 8: The a_1 channel fit result shown as projections in the tau and a_1 decay angles. This information corresponds to a small subset of the six-dimensional space used to make the measurement. The dashed (dotted) histogram is the Monte Carlo contribution from right- (left-) handed taus. The solid-line histogram indicates the sum of all Monte Carlo contributions.

$\cos\theta$ range	Polarisation		
	method CC	method NN	combined
$[-0.9, -0.7]$	-0.048 ± 0.055	-0.064 ± 0.056	-0.056 ± 0.053
$[-0.7, -0.5]$	-0.047 ± 0.056	-0.007 ± 0.053	-0.026 ± 0.051
$[-0.5, -0.3]$	-0.045 ± 0.059	-0.086 ± 0.060	-0.065 ± 0.056
$[-0.3, -0.1]$	-0.074 ± 0.064	-0.046 ± 0.063	-0.056 ± 0.060
$[-0.1, +0.1]$	-0.149 ± 0.065	-0.194 ± 0.067	-0.171 ± 0.063
$[+0.1, +0.3]$	-0.111 ± 0.062	-0.125 ± 0.062	-0.118 ± 0.059
$[+0.3, +0.5]$	-0.230 ± 0.059	-0.223 ± 0.056	-0.226 ± 0.054
$[+0.5, +0.7]$	-0.300 ± 0.052	-0.262 ± 0.053	-0.281 ± 0.050
$[+0.7, +0.9]$	-0.208 ± 0.054	-0.259 ± 0.052	-0.235 ± 0.050

Table 8: Measured polarisation as a function of polar angle, for the two single-tau methods and the combined result. The error is statistical only.

parameter	method CC	method NN	combined result
A_e	0.114 ± 0.026	0.119 ± 0.026	$0.117 \pm 0.025 \pm 0.008$
A_τ	0.138 ± 0.019	0.142 ± 0.019	$0.140 \pm 0.019 \pm 0.014$
$A_{e-\tau}$	0.127 ± 0.016	0.134 ± 0.016	$0.131 \pm 0.015 \pm 0.009$

Table 9: Uncorrected polarisation parameters extracted from polar angle fit, for the two single-tau methods with their statistical errors. For the combined result, the first error is statistical and the second is systematic.

parameter	single-tau result
$\mathcal{A}_e$	$0.120 \pm 0.025 \pm 0.008$
$\mathcal{A}_\tau$	$0.143 \pm 0.019 \pm 0.014$
$\mathcal{A}_{e-\tau}$	$0.134 \pm 0.015 \pm 0.009$

Table 10: Polarisation parameters extracted from the single-tau analysis. The first error is statistical, the second systematic.

polarisation in each bin, a 100 % correlated error on the polarisation between each of the nine bins. This correlated error between bins is simply the systematic error on A_τ without the Monte Carlo statistical error. The resulting systematic uncertainty on $A_{e-\tau}$ is 0.009. Table 9 shows the combined results for the angular fit from the two single-tau methods.

To infer from the measured parameters A_e, A_τ, and $A_{e-\tau}$ the values of $\mathcal{A}_e$, $\mathcal{A}_\tau$, and $\mathcal{A}_{e-\tau}$ at the Z peak one must correct for photon exchange and interference, and initial-state radiation. The calculated values of the corrections, totalling +0.003 for each of the parameters, result from comparing the values of the parameters obtained in a standard model calculation including and excluding these effects.

Ignoring the helicity correlations of the two taus in each event leads to a systematic underestimation of the statistical error on $\mathcal{A}_e$, $\mathcal{A}_\tau$ and $\mathcal{A}_{e-\tau}$. The statistical errors shown have been increased by the factor 1.023 to take this effect into account. The corrected results are given in table 10.

6 Acollinearity Method

6.1 Selection

The acollinearity analysis uses only events at the Z peak in which both taus decay into one charged track and the polar angles θ for those tracks satisfy $|\cos\theta| < 0.9$. The charged tracks are identified, and the decay channel classified using the NN method described in section 4. The events are classified into two categories, called the

- $\pi - X$, or "inclusive pion": at least one hemisphere is classified as $\tau \to \pi\nu$, and there is no restriction on the other tau hemisphere, and
- $l - X$ or "inclusive lepton": at least one hemisphere is classified as $\tau \to e\nu\overline{\nu}$ or $\tau \to \mu\nu\overline{\nu}$, and neither hemisphere is classified as $\tau \to \pi\nu$ in order to avoid double counting.

The overall acceptances and backgrounds of this selection, estimated from Monte Carlo simulation, appear in table 11. Figure 10 illustrates the acceptance as a function of acollinearity. The acollinearity distribution is corrected bin by bin for these effects.

6.2 Polarisation Extraction

To extract the polarisation from the acollinearity, the distributions are compared with a theoretical prediction, which is available in analytic form calculated at tree level with no

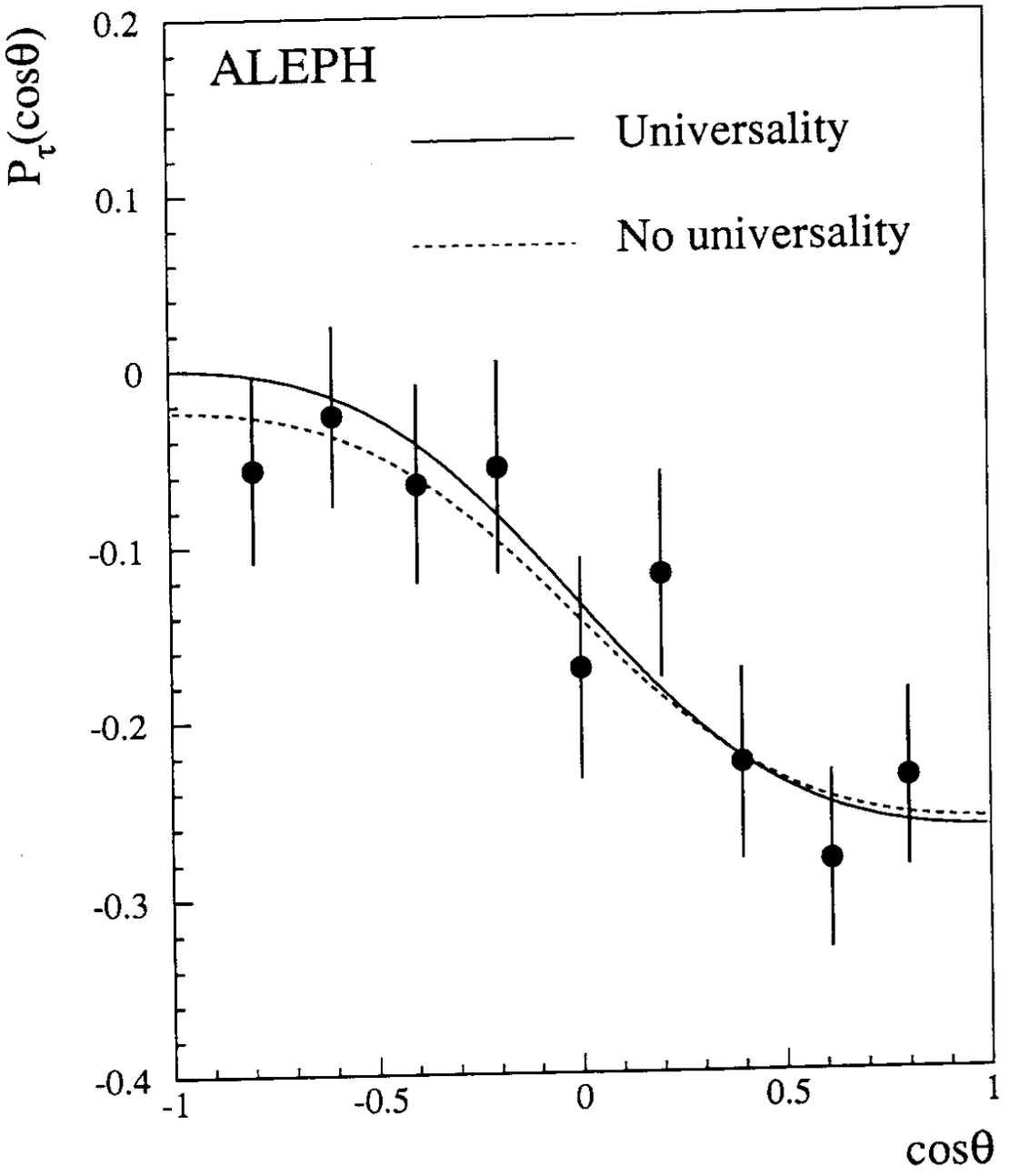

Figure 9: Measurement $P_\tau(\cos\theta)$ from the single-tau method. The solid (dashed) line shows the fit curve with (without) the assumption of tau-electron universality.

item	$\pi - X$	$l - X$
candidate events	1987	3699
acceptance (%)	60	55
tau background	6.4	6.2
non-tau background	0.9	0.9

Table 11: Summary of the efficiencies and backgrounds (in percent) for the selected acollinearity sample.

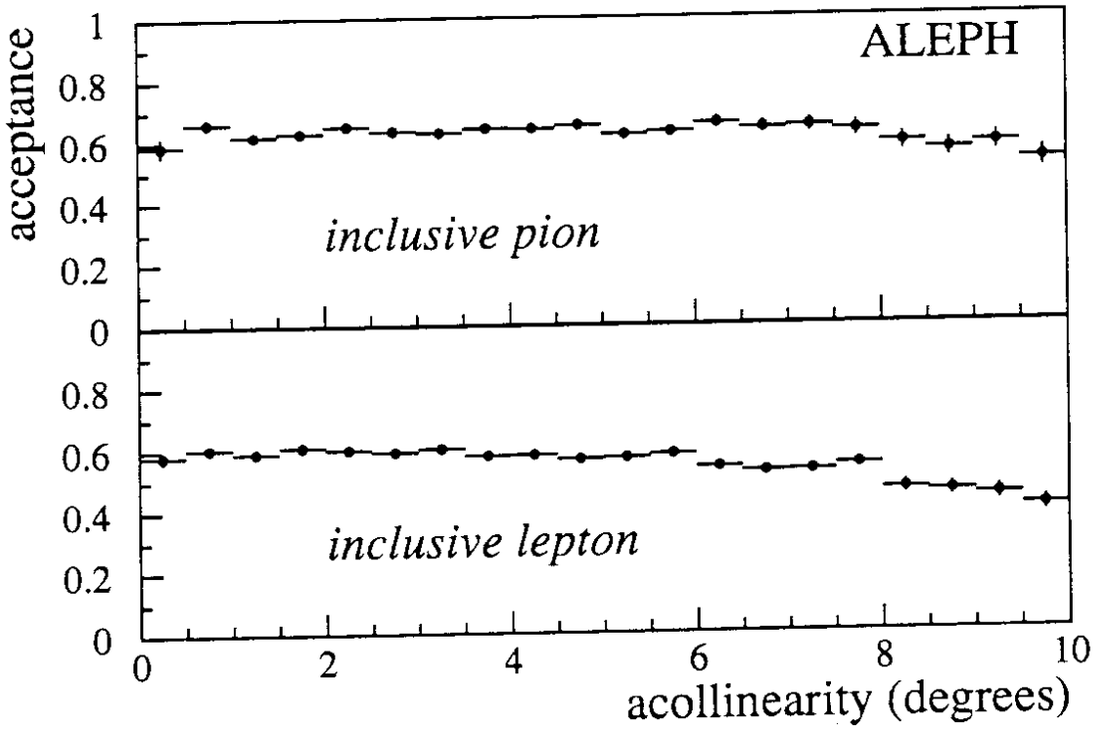

Figure 10: Absolute acceptance for the two acollinearity samples as a function of the acollinearity.

initial- or final-state radiation [6]. The measured distributions are corrected for angular resolution and radiative effects. The corrected number of events in a given acollinearity bin i is given by

$$N_i^{\rm cor} = C_i^{\rm rad} \frac{1}{\eta_i} \sum_j A_{ij} N_j^{\rm obs} (1 - B_j) \tag{14}$$

where $N_j^{\rm obs}$ is the number of events in bin j of acollinearity, η_i and B_j refer to the efficiencies and background fractions and $C_i^{\rm rad}$ is a correction factor accounting for radiative effects and the effect of accompanying neutral particles. The angular resolution unfolding matrix A_{ij} has been calculated from the bin to bin migrations observed in Monte Carlo events with full detector simulation by solving the equation

$$O_i = \sum_j G_{ij} \cdot T_j \tag{15}$$

where O_i is the number of events in acollinearity bin i, T_j is the number of events in bin j of the true acollinearity, and $G_{ij} = A_{ij}^{-1}$ is the probability that an event with true acollinearity ε in bin j will be reconstructed with observed acollinearity in bin i. Inverting the matrix G_{ij} can in principle lead to unstable results. This is not the case in this analysis for which G_{ij} is nearly diagonal.

The coefficients $C_i^{\rm rad}$ have been derived from two high-statistics Monte Carlo samples of tau pair events generated without detector simulation [3]. One sample was generated on the peak of the Z resonance with all radiative effects disabled, while the other was generated with full radiative effects. The corrections are calculated as the ratio of the differential acollinearity distributions of these two samples.

6.3 Systematic Uncertainties

The major contributions to the systematic errors on the polarisation measured from the acollinearity distributions appear in table 12. They come from the determination of the correction coefficients, the selection, the branching ratios and detector effects.

One main source of uncertainty arises from the slight dependence on P_τ observed in the determination of the $C_i^{\rm rad}$ coefficients used in the fitting procedure. The systematic uncertainty quoted is derived by varying P_τ by the statistical error of the measurement.

The selection efficiency has been verified with data using Bhabha and dimuon events for the low acollinearity range and two photon interactions for high acollinearities. No discrepancies with respect to the simulation are found within the statistical precision. The normalization and shape of the background are varied by changing the tau branching ratios by $\pm 15\%$ and the normalization of the non-tau background by $\pm 20\%$.

As the event samples used are inclusive, uncertainties in the branching ratios, needed to compute the theoretical acollinearity distributions, lead to systematic uncertainties labeled "model dependence" in table 12.

The acollinearity angle distribution is measured exclusively from track angles. Therefore, detector effects in the acollinearity are largely independent from those of the single-tau method which relies mainly on energy measurements. Possible rotation of the TPC endplates, leading to shifts in the azimuthal angle, is studied using $Z \rightarrow \mu^+\mu^-$ events and is

source	$\pi - X$	$l - X$
$C^{\rm rad}(P_\tau)$	0.007	0.004
selection	0.008	0.008
backgrounds	0.009	0.005
model dependence	0.008	0.014
tracking	0.001	0.003
total	0.016	0.018

Table 12: Summary of systematic errors on P_τ (and equivalently $\mathcal{A}_\tau$) for the two event categories of the acollinearity method.

$\cos\theta$ range	P_τ
$[-0.9, 0.]$	-0.038 ± 0.078
$[0., +0.9]$	-0.254 ± 0.078

Table 13: Measured polarisation as a function of polar angle, for the acollinearity method. The error is statistical only.

smaller than 0.04 mrad. The TPC drift velocity, which enters directly into the determination of the polar angle, is known to a relative accuracy of 3.5×10^{-4} by comparing the track extrapolation in the ALEPH vertex detector with their actual measured hits. This implies a relative uncertainty in the component of track momentum along the drift direction of the same size and can affect the acollinearity. Other effects related to distortions of TPC tracks have been shown to be negligible.

The uncertainties introduced by limited Monte Carlo statistics affect only the acceptance and are included in the statistical errors for the corrected data. Finally, theoretical uncertainties in equation 8 contribute less than 0.001 to the systematic errors.

6.4 Acollinearity Method Results

In the acollinearity method the values of $\mathcal{A}_e$ and $\mathcal{A}_\tau$ are obtained from P_τ measured in the forward and backward hemispheres. The values of P_τ are extracted from the corrected acollinearity distributions of the inclusive pion and inclusive lepton samples, shown in figure 11. Correlations between bins due to the unfolding procedure are taken into account. The range of 0 to 10 degrees is used for both selected samples. Outside that range the cross section is very small and the systematic uncertainties in the unfolding procedure large.

Table 13 shows the values of P_τ obtained in the forward and backward hemispheres; only these two bins in polar angle are used on account of limited statistics. The solid curves in figure 11 show the acollinearity distributions corresponding to these values.

Table 14 shows the corresponding values of $\mathcal{A}_e$ and $\mathcal{A}_\tau$, or, assuming universality, $\mathcal{A}_{e-\tau}$, extracted using equation 1. The correlation between $\mathcal{A}_e$ and $\mathcal{A}_\tau$ is about 0.06. The systematic error on $\mathcal{A}_{e-\tau}$ is calculated using the same procedure as for the single-tau method. These results are combined in the next section with the corresponding values obtained from the single-tau method. This method, in contrast to the single-tau method, takes the

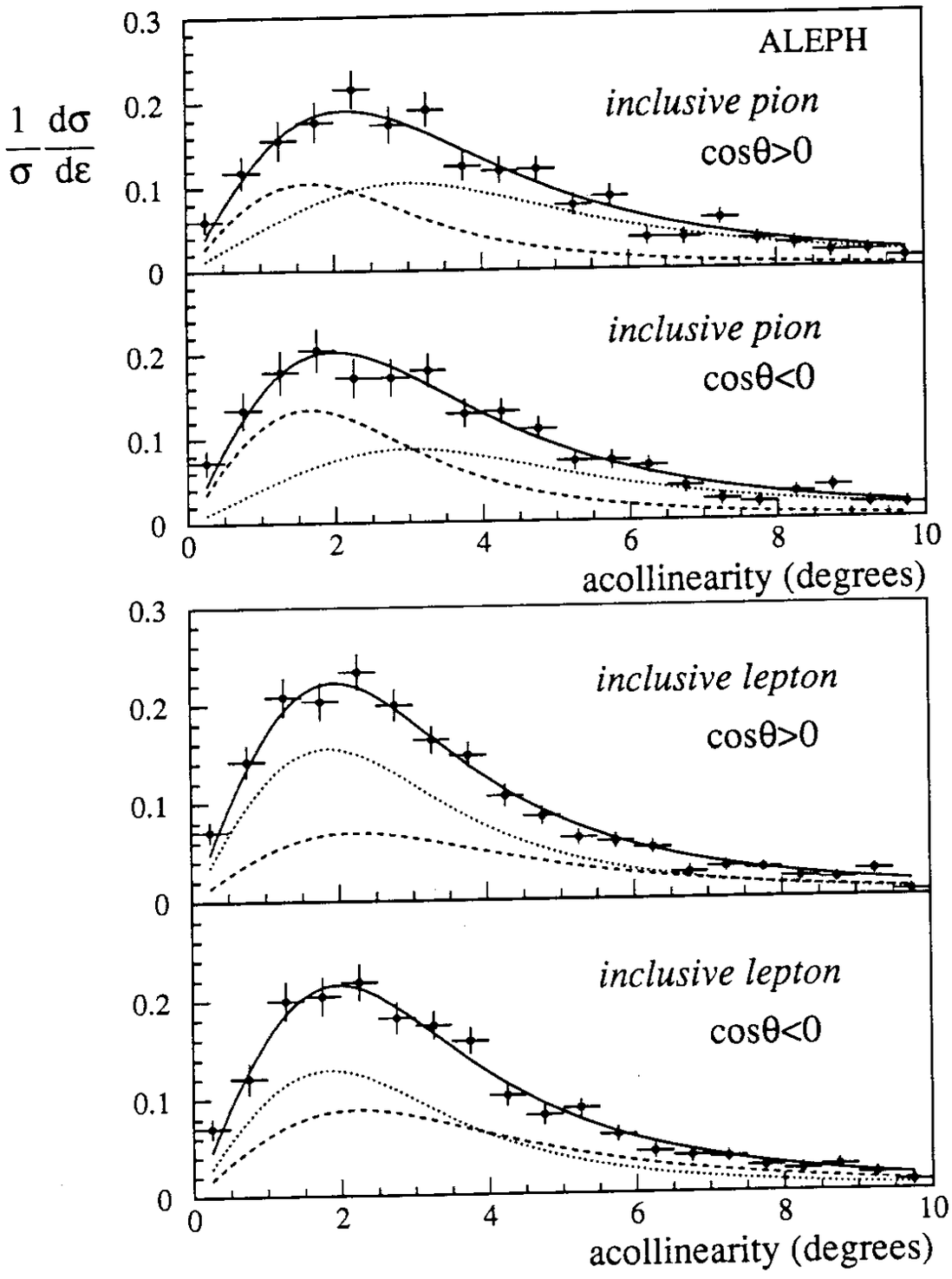

Figure 11: Result of the fits to the normalized forward and backward cross sections as function of the acollinearity. The points with error bars are the data corrected for acceptance, background, and radiative effects. Solid curves are the result of the fits. Dashed (dotted) curves are the contributions from right- (left-) handed taus.

parameter	acollinearity result
$\mathcal{A}_e$	$0.154 \pm 0.079 \pm 0.002$
$\mathcal{A}_\tau$	$0.147 \pm 0.056 \pm 0.011$
$\mathcal{A}_{e-\tau}$	$0.149 \pm 0.047 \pm 0.009$

Table 14: Polarisation parameters extracted from polar angle dependence of the acollinearity distribution. The first error is statistical and the second is systematic.

parameter	final result
$\mathcal{A}_e$	$0.120 \pm 0.025 \pm 0.008$
$\mathcal{A}_\tau$	$0.143 \pm 0.019 \pm 0.014$
$\mathcal{A}_{e-\tau}$	$0.134 \pm 0.015 \pm 0.009$

Table 15: Polarisation parameters extracted from polar angle dependence, combining the single-tau method results with those of the acollinearity method. The first error is statistical and the second is systematic.

initial- and final-state radiative corrections into account by means of the deconvolution coefficients. Since this method uses data only at the Z peak other corrections are negligible.

7 Combined Results

One can combine the results for $\mathcal{A}_e$, $\mathcal{A}_\tau$, and $\mathcal{A}_{e-\tau}$ from the single-tau and acollinearity methods in a weighted average, taking into account the correlations between them [15]. The statistical correlation coefficient relating the results from the two methods is 0.5 when the measurements are performed on the same data sample. The actual correlation coefficient is 0.3, however, since the acollinearity measurement is made only for data collected at the peak of the Z resonance. The correlation of the single-tau and acollinearity systematic errors is negligible. The final combined results appear in Table 15.

8 Interpretation and Conclusion

The results presented so far are the basic physical quantities measured in this analysis of the polarisation of taus in Z decay. They are compatible with and improve the published ALEPH results [2] as well as the results from other LEP experiments [17]. The comparison of $\mathcal{A}_e$ and $\mathcal{A}_\tau$ shows that universality between electron and tau in neutral currents holds well.

Combining the statistical and systematic errors in quadrature, the results are

$$\mathcal{A}_e = 0.120 \pm 0.026, \quad (16)$$

$$\mathcal{A}_\tau = 0.143 \pm 0.023, \quad (17)$$

$$\mathcal{A}_{e-\tau} = 0.134 \pm 0.018. \quad (18)$$

From these measurements one can infer the ratios of the vector and axial-vector couplings of the Z to leptons by using the relation of equation 2, with the results

$$\frac{g_V^e}{g_A^e} = +0.060 \pm 0.013, \tag{19}$$

$$\frac{g_V^\tau}{g_A^\tau} = +0.072 \pm 0.012, \tag{20}$$

$$\frac{g_V^{e-\tau}}{g_A^{e-\tau}} = +0.067 \pm 0.009. \tag{21}$$

The data support the hypothesis of electron-tau universality in the neutral current:

$$\frac{g_V^e}{g_A^e} / \frac{g_V^\tau}{g_A^\tau} = 0.85 \pm 0.27. \tag{22}$$

This result brings new information on the vector couplings since the Z axial couplings are known to verify universality to much higher precision [7] through measurement of the Z partial decay widths.

Using the relation

$$\sin^2 \theta_W^{\rm eff} \equiv \frac{1}{4}\left(1 - \frac{g_V^l}{g_A^l}\right), \tag{23}$$

the effective weak mixing angle at the Z mass is

$$\sin^2 \theta_W^{\rm eff} = 0.2332 \pm 0.0022. \tag{24}$$

Acknowledgements

We wish to express our thanks to the LEP Division, whose efforts towards continuous improvement of the accelerator have borne fruit in this work. We thank also the engineers and support personnel at our home institutions for contributing to the success of the experiment. Finally those of us who are guests at CERN thank the laboratory for its hospitality and support.

References

[1] S. Jadach *et al.*, Z Physics at LEP I, CERN 89-08, eds. G. Altarelli, *et al.*, vol. 1, 235 (1989).

[2] D. Decamp *et al.*, ALEPH Collab., Phys. Lett. **B265**, 430 (1991).

[3] S. Jadach, B.F.L. Ward, and Z. Was, Comp. Phys. Comm. **66** (1991) 276. KORALZ version 3.8;
S. Jadach, J.H. Kühn, and Z. Was, Comp. Phys. Comm. **64** (1991) 275;
Z. Was and S. Jadach, CERN-TH 6727/92.

[4] Y.S. Tsai, Phys. Rev. **D4**, 2821 (1971).

[5] M. Davier, L. Duflot, F. Le Diberder, A Rougé, "The optimal method for the measurement of tau polarisation". Preprint LAL 92-73 or X-LPNHE 92-22.

[6] R. Alemany, N. Rius, J. Bernabeu, J.J. Gomez-Cadenas, A. Pich, Nucl. Phys. **B379**, 3 (1992).

[7] D. Buskulic *et al.*, ALEPH Collab., CERN-PPE/93-40, submitted to Z. Phys. C.

[8] D. Decamp *et al.*, ALEPH Collab., Nucl. Inst. Meth. **A294**, 121 (1990).

[9] L. Lönnblad *et al.*, Comp. Phys. Comm. **70**, 167 (1992).

[10] D. Decamp *et al.*, ALEPH Collab., Phys. Lett. **B284**, 17 (1992);
S. Snow, Proceedings of the Second Workshop on Tau Lepton Physics, Columbus, Ohio 8-11 September, 1992.

[11] J.H. Kühn and E. Mirkes, Phys. Lett. **B286**, 381 (1992);
J.H. Kühn and E. Mirkes, Z. Phys. C56, 661, (1992).

[12] N. Isgur *et al.*, Phys. Rev. **D39**, 1357 (1989).

[13] M. Feindt, Z. Phys **C48**, 681 (1990).

[14] H. Albrecht *et al.*, DESY 92-125 (1992).

[15] L. Lyons, D. Gibaut, and P. Clifford, Nucl. Inst. Meth. **A270**, 110 (1988).

[16] A. Rougé, "Tau Decays as Polarization Analyzers," Proceedings of the Workshop on Tau Lepton Physics, 24-27 September 1990, eds. M. Davier and B. Jean-Marie, Orsay, France.

[17] P. Abreu *et al*, DELPHI Collab., Z. Phys **C55** 555 (1992);
O. Adriani *et al*, L3 Collab., Phys. Lett. **B294** 466 (1992);
G. Alexander *et al*, OPAL Collab., Phys. Lett. **B266** 201 (1991).

Appendix A

The variable ω expresses the fractional difference between the probability densities of the tau decay having originated from a positive or negative helicity tau[2]. Thus

$$\omega = \frac{W^+(\vec{\xi}) - W^-(\vec{\xi})}{W^+(\vec{\xi}) + W^-(\vec{\xi})}, \tag{25}$$

where $W^{\pm}(\vec{\xi})$ represents the theoretical expression for the decay distribution for a τ of helicity $\pm\frac{1}{2}$ and $\vec{\xi}$ the set of all the decay observables: energies or angles.

[2]By convention, the helicity is used here for the τ^- and minus the helicity for the τ^+.

In the case of a hadronic decay, the τ decay angle ψ_τ is related to the total hadronic energy E_h by

$$\cos\psi_\tau = \frac{2E_h/E_{beam} - 1 - m^2/m_\tau^2}{1 - m^2/m_\tau^2}, \tag{26}$$

where m is the mass of the hadronic system. Its distribution is [4]

$$W^\pm(\cos\psi_\tau) = \frac{1}{2}[1 \pm \alpha\cos\psi_\tau], \tag{27}$$

with $\alpha = 1$ for spin 0 particles (pion) and $\alpha = (m_\tau^2 - 2m^2)/(m_\tau^2 + 2m^2)$ for spin 1 particles (ρ, a_1).

The reduction of the analysing power by the factor α in the case of a spin 1 hadron is due to the presence of several helicity states. It can be overcome by measuring the hadron helicity through its decay distribution.

If $\vec{\zeta}$ is the set of observables in the hadron decay, the complete decay distribution is a function of ψ_τ and $\vec{\zeta}$:

$$W^\pm = \frac{3}{4(m_\tau^2 + 2m^2)}[w_1^\pm(m,\psi_\tau)h_1(\vec{\zeta}) + w_0^\pm(m,\psi_\tau)h_0(\vec{\zeta}) + w_{-1}^\pm(m,\psi_\tau)h_{-1}(\vec{\zeta})]. \tag{28}$$

The lower index represents the hadron helicity in the laboratory; h_λ is the decay distribution for a hadron of helicity λ. Let us stress the fact that the helicity in the laboratory is not the same as the helicity in the τ rest frame.

The functions $w_0^\pm$, $w_1^\pm$ and $w_{-1}^\pm$ are elements of the hadron density matrix they are given in [16]:

$$\begin{aligned} w_0^+ &= [m_\tau\cos\eta\cos\frac{\psi_\tau}{2} + m\sin\eta\sin\frac{\psi_\tau}{2}]^2 \\ w_0^- &= [m_\tau\cos\eta\sin\frac{\psi_\tau}{2} - m\sin\eta\cos\frac{\psi_\tau}{2}]^2 \end{aligned} \tag{29}$$

$$\begin{aligned} w_1^+ + w_{-1}^+ &= [m_\tau\sin\eta\cos\frac{\psi_\tau}{2} - m\cos\eta\sin\frac{\psi_\tau}{2}]^2 + m^2\sin^2\frac{\psi_\tau}{2} \\ w_1^- + w_{-1}^- &= [m_\tau\sin\eta\sin\frac{\psi_\tau}{2} + m\cos\eta\cos\frac{\psi_\tau}{2}]^2 + m^2\cos^2\frac{\psi_\tau}{2} \end{aligned} \tag{30}$$

$$\begin{aligned} w_1^+ - w_{-1}^+ &= 2m\sin\frac{\psi_\tau}{2}[m_\tau\sin\eta\cos\frac{\psi_\tau}{2} - m\cos\eta\sin\frac{\psi_\tau}{2}] \\ w_1^- - w_{-1}^- &= 2m\cos\frac{\psi_\tau}{2}[m_\tau\sin\eta\sin\frac{\psi_\tau}{2} + m\cos\eta\cos\frac{\psi_\tau}{2}] \end{aligned} \tag{31}$$

Their somewhat intricate expressions are due to the Wigner rotation η between the two above mentioned helicity frames. Neglecting $\mathcal{O}(m_\tau^2/M_Z^2)$ terms,

$$\tan\frac{\eta}{2} = \frac{m}{m_\tau}\tan\frac{\psi_\tau}{2} \tag{32}$$

In the case of the ρ, the only observable is $\cos\psi_\rho$ where ψ_ρ is the angle between the direction of the charged π and the axis defined by the direction of the laboratory viewed from the ρ rest frame.

Since $\cos\psi_\rho$ is a scalar quantity, it cannot distinguish between the helicities $+1$ and -1 of the ρ. The functions h are

$$\begin{aligned} h_1 = h_{-1} &= \sin^2\psi_\rho \\ h_0 &= 2\cos^2\psi_\rho \end{aligned} \tag{33}$$

In the case of the a_1 the decay observables are the two-pion effective masses m_{ij} and two angles ψ_a and γ_a defined as follows [11]. In the a_1 rest frame, the z axis is chosen perpendicular to the plane made by the three pion momenta and the x axis along the direction of the unlike-charge pion. The angles ψ_a and γ_a are the polar and azimuthal angles of the direction of the laboratory viewed from the a_1 rest frame.

Here the quantity $\cos\psi_a$ is pseudoscalar and the decay distribution contains a term linear in $\cos\psi_a$ which allows the distinction between the $+1$ and -1 helicities of the a_1. The relevant (unnormalized) decay functions are

$$\begin{aligned} h_0 &= W_A \sin^2\psi_a + W_C \sin^2\psi_a \cos 2\gamma_a - W_D \sin^2\psi_a \sin 2\gamma_a \\ h_1 + h_{-1} &= W_A(1+\cos^2\psi_a) - W_C \sin^2\psi_a \cos 2\gamma_a + W_D \sin^2\psi_a \sin 2\gamma_a \\ h_1 - h_{-1} &= 2W_E \cos\psi_a \end{aligned} \tag{34}$$

The dependence on the m_{ij}'s is embodied in the "structure functions" [11] W_A, W_C, W_D, and W_E. They can be computed from the complex amplitude which describes the dynamics of the a_1 decay. Therefore some model dependence enters through the W's in the ω definition.

Due to the Pauli principle, W_E is an odd function whose integral over the Dalitz plot is zero. After integration over the Dalitz plot and on γ_a, only W_A survives and can be absorbed in the normalization, resulting in the model independent distribution used in our earlier analysis [2]

$$\begin{aligned} h_1 = h_{-1} &= \frac{1+\cos^2\psi_a}{2} \\ h_0 &= \sin^2\psi_a \end{aligned} \tag{35}$$

Using the energies as polarisation analysers, the decay distributions of τ^+ and τ^- have the same form when expressed in terms of the τ^- polarisation ($P = P_{\tau^-} = -P_{\tau^+}$). This property is shared by all decay distributions involving only scalar observables for the polarisation appears then through the product χP, where χ is the handedness of the neutrino produced in the decay. That is not true when pseudoscalar observables are used; the coefficient $w_1^\pm - w_{-1}^\pm$ of the term in $\cos\psi_a$ has opposite signs for τ^+ and τ^-.

Note that the τ decay angle ψ_τ is θ in the references [2], [16] and [11]. The angle ψ_ρ is ψ in [2] and [16]. The angle ψ_a is ψ in [2] and [16], β in [11]. The angle γ_a is γ in [11]. The angle η is ψ in [11] and η in [16].

Appendix B

The functions $F(\varepsilon)$ and $G(\varepsilon)$ of the acollinearity angle ε can be defined as follows:

$$F(\varepsilon) = Q_{11}(\varepsilon) + \alpha_1\alpha_2 Q_{22}(\varepsilon), \tag{36}$$

$$G(\varepsilon) = \alpha_1 Q_{21}(\varepsilon) + \alpha_2 Q_{12}(\varepsilon), \tag{37}$$

where the subscripts 1 and 2 refer to the event hemispheres and the coefficient α_i is the analyzing power of the decay in hemisphere i, and the Q_{ij} functions reflect the kinematics of the combination of tau decay modes in the two hemispheres. The integral over ε of $F(\varepsilon)$ is unity whereas the integral of $G(\varepsilon)$ is zero.

The functions $Q_{ij}(\varepsilon)$ are defined as in [6]

$$\begin{aligned} Q_{ij}(\varepsilon) \equiv\ & 4\pi \sin\varepsilon \int \frac{E_1^* E_2^*}{Q'}\ q_1\ q_2\ dE_1 d\cos\theta_1 dE_2 d\cos\theta_2 \cdot \\ & A_i^1 \cdot (q_1^* \cos\theta_1^*)^{i-1} A_j^2 \cdot (q_2^* \cos\theta_2^*)^{j-1} \end{aligned} \tag{38}$$

The $A_m^{1(2)}$ are the decay distribution functions [4], where m refers to the decay mode and superscript 1 refers to scalar term of the tau partial width for that decay mode and superscript 2 refers to the spin-dependent term. Also q_i, θ_i and E_i are the momentum, direction and energy of the τ decay products in hemisphere i in the laboratory frame respectively. The label * refers these quantities to the τ rest frames.

Finally, Q' is given by

$$Q' = \sqrt{\sin^2\theta_1 \sin^2\theta_2 - (\cos\theta_1 \cos\theta_2 - \cos\varepsilon)^2}. \tag{39}$$